REPORT DOCUMENTATION PAGE

Form Approved
OMB No. 0704-0188

Public reporting burden for this collection of information is estimated to average 1 hour per response, including the time for reviewing instructions, searching existing data sources, gathering and maintaining the data needed, and completing and reviewing this collection of information. Send comments regarding this burden estimate or any other aspect of this collection of information, including suggestions for reducing this burden to Department of Defense, Washington Headquarters Services, Directorate for Information Operations and Reports (0704-0188), 1215 Jefferson Davis Highway, Suite 1204, Arlington, VA 22202-4302. Respondents should be aware that notwithstanding any other provision of law, no person shall be subject to any penalty for failing to comply with a collection of information if it does not display a currently valid OMB control number. **PLEASE DO NOT RETURN YOUR FORM TO THE ABOVE ADDRESS.**

1. REPORT DATE *(DD-MM-YYYY)*	2. REPORT TYPE	3. DATES COVERED *(From - To)*
06-09-2013	Final Report	August, 2010 - July 2013

4. TITLE AND SUBTITLE	5a. CONTRACT NUMBER
Characterizations of Nanofluid Heat Transfer Enhancements	
	5b. GRANT NUMBER
	AFOSR FA9550-10-1-0447
	5c. PROGRAM ELEMENT NUMBER

6. AUTHOR(S)	5d. PROJECT NUMBER
Johnson, Drew, W	
	5e. TASK NUMBER
	5f. WORK UNIT NUMBER

7. PERFORMING ORGANIZATION NAME(S) AND ADDRESS(ES)	8. PERFORMING ORGANIZATION REPORT NUMBER
Department of Civil & Environmental Engineering University of Texas at San Antonio One UTSA Circle San Antonio, TX 78249	

9. SPONSORING / MONITORING AGENCY NAME(S) AND ADDRESS(ES)	10. SPONSOR/MONITOR'S ACRONYM(S)
Air Force Office of Scientific Research 875 North Randolph Street, Suite 325, Room 3112, Arlington, VA., 22203-1768	AFOSR
	11. SPONSOR/MONITOR'S REPORT NUMBER(S)
	AFOSR FA9550-10-1-0447

12. DISTRIBUTION / AVAILABILITY STATEMENT

APPROVED FOR PUBLIC RELEASE, DISTRIBUTION UNLIMITED

13. SUPPLEMENTARY NOTES

14. ABSTRACT

Nanoparticle morphology is thought to be an important factor influencing heat and mass transfer rates in liquid systems. How nanoparticles mechanistically increase heat and mass transfer rates is not well understood. Both dispersed nanoparticles and aggregated nanoparticles are thought to play important roles. Dispersed nanoparticles and associated nanoparticle Brownian movements are purported to cause the enhancements by mixing mechanisms whereas aggregated nanoparticles are purported to cause enhancements by forming highly conductive paths. In this study, morphologies of nanoparticle were quantified in laboratory studies and related to laboratory measured heat and mass transfer rates. No mass transfer enhancements were found in the presence of nanoparticles. Thermal conductivity could be predicted with effective medium theory when aggregated nanoparticle aspect ratio was considered.

15. SUBJECT TERMS

16. SECURITY CLASSIFICATION OF:			17. LIMITATION OF ABSTRACT	18. NUMBER OF PAGES	19a. NAME OF RESPONSIBLE PERSON
a. REPORT	b. ABSTRACT	c. THIS PAGE			19b. TELEPHONE NUMBER *(include area code)*

Standard Form 298 (Rev. 8-98)
Prescribed by ANSI Std. Z39.18

Final Report for FA9550-10-1-0447: "Characterizations of Nanofluid Heat Transfer Enhancements"

Drew W. Johnson, PhD PE

Associate Professor
Civil & Environmental Engineering
University of Texas at San Antonio

Executive Summary

Nanoparticle morphology is thought to be an important factor influencing heat and mass transfer rates in liquid systems. How nanoparticles mechanistically increase heat and mass transfer rates is not well understood. Both dispersed nanoparticles and aggregated nanoparticles are thought to play important roles. Dispersed nanoparticles and associated nanoparticle Brownian movements are purported to cause the enhancements by mixing mechanisms whereas aggregated nanoparticles are purported to cause enhancements by forming highly conductive paths. In this study, morphologies of nanoparticle were quantified in laboratory studies and related to laboratory measured heat and mass transfer rates.

Grant research objectives were to answer fundamental questions related to mechanisms of nanofluid heat transfer enhancer enhancements. Activities in part (1) were designed to answer the question of: Are enhancements related to Brownian nanoparticle motion? Activities in part (2) were conducted to answer the question of: Are enhancements related to the extent of particle aggregation and morphology of aggregated particles, and if so, can the extent of particle aggregation and associated heat transfer enhancements be characterized using fractal dimensions of aggregated nanoparticles? Study parts (1) and (2) comprise the majority of the research effort to satisfy objectives associated with rational for funding support. Additional activities in the final year of the grant were completed once these major research objectives had been met. In study part (3), the morphology characterization techniques developed to study heat transfer mechanisms were extended and employed to quantify nanoparticle morphology effects on nanoparticle filtration behaviors. Finally, in study part (4), heat transfer enhancements and viscosities of large aspect ratio nanoplatelets nanofluids were measured. These activities were an attempt to utilize findings of study part (2) and investigate nanofluids with potentially large thermal conductivity enhancements.

Key Findings of Study Part 1:

No mass transfer enhancements were found in the presence of nanoparticles. Oxygen transfer was actually diminished at the highest nanoparticle volume fraction; this is attributed to solution

viscosity effects and the obstruction effects of impermeable nanoparticles. No evidence was found to substantiate the purported Brownian motion micro/nano-scale convection effect of nanoparticles that has been used by others to explain anomalous heat and mass transfer rates in nanofluids.

Key Findings of Study Part 2:

Fractal dimensions and aspect ratios were used to quantify the aggregation morphologies. Fractal dimensions were measured using static light scattering and imaging techniques. Aspect ratios were measured using dynamic light scattering, scanning electron microscopy and atomic force microscopy. Results showed that the enhancements in thermal conductivity can be predicted with effective medium theory when aspect ratio was considered.

Key Findings of Study Part 3:

Nanoparticles were aggregated under conditions of high and low ionic strength to form aggregates of different morphology. Aggregates were filtered using a hydrophilic Polyvinylidene fluoride (PVDF) membrane with a pore size 0.22 μm and 100% nanoparticle removal efficiencies were obtained regardless of aggregation conditions used. Aggregate morphology was quantified by measured fractal dimensions. Fractal structure differences coincided with measured filtration resistance values. Low porosity aggregates provided a filtration resistance 43% greater than high porosity aggregates of the same effective size. Model predictions for measured specific resistance values were improved through incorporation of compressibility indexes. In order to obtain a porous structure with less resistance, a fast coagulation process is suggested for nanoparticle removal.

Key Findings of Study Part 4:

Graphene nanoplatelets (Diameter ~5μm, Thickness of 2-10nm) at a loading of 27 g L^{-1} were sonicated in a 2% w/v sodium cholate DI water solution. Sodium cholate surfactant was used to prevent graphene aggregation. The resulting exfoliated graphene platelet nanofluid was subsequently centrifuged to provide a stable suspension suitable for thermal conductivity and solution viscosity measurements at different platelet volume fractions. The highest volume fraction achieved of 0.0027 (after 9 hours of sonication) provided a thermal conductivity enhancement of 8% with viscosity essentially unchanged and equivalent to water. Measured enhancements in thermal conductivity agree within 6% of effective medium theory predictions based upon nanoplatelet morphologies determined from SEM imaging.

Study Details Are Provided in The Following Publications:

Feng, X. and Johnson, D. W. (2012) "Mass Transfer in SiO2 Nanofluids: A Case against Purported Nanoparticle Convection Effects" International Journal of Heat and Mass Transfer Journal, 55, 3447–3453

Feng, X. (2012). Nanoparticle morphology effects in heat and mass transfer processes, PhD Dissertation, The University of Texas at San Antonio.

Feng, X. and Johnson, D. W. (2013) "Characterization of Dispersed and Aggregated Al_2O_3 Morphologies for Predicting Nanofluid Thermal Conductivities" Journal of Nanoparticle Research, 13,6 1-11

Feng, X. and Johnson, D. W. (2013), "Aggregated Nanoparticle Morphology Effects on Membrane Filtration", Chemical Engineering Communications, submitted for publication September 2013

Bahaya, B. (2013-In Preparation). Heat Transfer Enhancements and Viscosities of Nanofluids Comprised of Large Aspect Ratio Nanoplatelets, The University of Texas at San Antonio.

Study Details Were Provided in The Following Presentations:

Drew Johnson, Xuemei Feng, Nanoparticle Morphology Effects in Membrane Filtration", the 23rd Annual Meeting of the North American Membrane Society, Boise ID, June 2013

Drew Johnson, Xuemei Feng, "Nanoparticle morphology effects in heat and mass transfer processes" Southwest Research Institute, San Antonio, TX, January 8th 2013.

Xuemei Feng, Drew Johnson, "Experimental Investigation of Nanofluid Brownian Motion and Aggregation Effects on Transport Processes", ASME International Mechanical Engineering Congress & Exposition, Denver, CO, November 11-17, 2011

Xuemei Feng, Drew Johnson, "Mass Transfer Measurements to Characterize Nanofluid Transport Mechanisms", ASME International Mechanical Engineering Congress & Exposition, Denver, CO, November 11-17, 2011

Drew Johnson, Xuemei Feng, Mass Transfer Measurements to Characterize Nanofluid Transport Mechanisms, United States Air Force Office of Scientific Research Thermal Program review in Arlington, Virginia, September 26-28, 2011

Drew Johnson, Xuemei Feng, "Characterization of Nanofluid Heat Transfer Enhancements", United States Air Force Office of Scientific Research Thermal Program review, Dayton, Ohio, October 13-14, 2010

Xuemei Feng, Drew Johnson, "Characterization of Nanofluid Mass Diffusivity", United States Air Force Office of Scientific Research Thermal Program review, Dayton, Ohio, October 13-14, 2010

The following students were supported with research funding provided through this grant:

Bernard Bahaya, MS Student, Civil & Environmental Engineering, University of Texas San Antonio, Expected Graduation is fall 2013.

Xuemei Feng, PhD Student, Environmental Engineering and Science, University of Texas San Antonio, Graduated Fall 2012.

Part (1): Are enhancements related to Brownian nanoparticle motion?

Brownian motion effects were experimentally explored by studying effects of non-aggregating spherical SiO2 nanoparticles on oxygen and NaCl mass transfer rates. No mass transfer enhancements were found in the presence of nanoparticles. Oxygen transfer rates were actually diminished by 30% at the highest nanoparticle volume fraction; this is attributed to solution viscosity effects (22% reduction associated with lower liquid film transfer coefficients) and the obstruction effects of impermeable nanoparticle (8% reduction). No evidence was found to

substantiate the purported Brownian motion micro/nano-scale convection effects often used by others to explain increased heat and mass transfer rates associated with nanoparticles in liquid systems.

1.1. Experimental Methods

1.1.1. Nanoparticle Characterization

The nanoparticles used in this study were spherical SiO_2 nanoparticles (manufacturer nominal size 13.7 ± 2 nm and 22.5 ± 2.5 nm, Microspheres-Nanospheres, Cold Springs, NY, 149011-05, 149015-05). Equivalent spherical diameters of nanoparticles used were measured using a dynamic light scattering method through Delsa Nano C (Beckman Coulter Inc, Brea, CA) with 658 nm laser and scattering angle 165°. The measured average diameters in NaCl mass transfer study were 17.2 ± 1.0 and 22.5 ± 1.5 nm. For the oxygen mass transfer study, measured average diameters were 20.0 ± 1.1 and 24.5 ± 2.4 nm. Nanoparticle size differences between the oxygen transfer study and the NaCl study may be due to different batches used from the manufacturer and also storage time differences between uses. Measured nanoparticle sizes did not change after thirty-four hours of incubation in the experimental conditions used, and sizes were stable over the duration of the experiments. To verify the sizes were stable, nanoparticles were diluted to 5% in the diffusion cell fitted with a PC membrane with initial low and high Cl^- concentration at 100 and 3000 ppm, respectively. The sizes of nanoparticles were intermittently measured over 34 hours and found to be of constant size.

1.1.2. Adsorption Assessment

Adsorption tests were conducted to verify that the membrane and nanoparticles were non-interacting with the chloride. Concentrations of Cl^- were compared before and after adding membrane or nanoparticles. Details for adsorption assessment are as follows. for membrane adsorption measurements, 13 mm circular polycarbonate membranes (Membrane solutions, Plano, TX, MFPC013040) were placed in 40 mL borosilicate glass vials containing 5.2 mL of 0.01, 0.025, 0.05 and 0.1 M NaCl. NaCl solutions were made by dissolving desired amounts of ACS grade NaCl (Thermo Fisher Scientific Inc., Pittsburgh, PA, 7647-14-5) into nanopure water of resistivity 18.2 MΩ cm. For nanoparticle adsorption assessment, 5.2 mL of 0.5 % nanofluid was prepared at the same NaCl concentrations. The concentration of chloride was recorded using a calibrated ion selective electrode (ISE) (Thermo Fisher Scientific Inc., Pittsburgh, PA, 13-620-527) at the beginning of the experiment, and after shaking at 70 rpm for 50 hours at 25 °C.

1.1.3. Diffusion Cell Measurements

The membrane diffusion cell (PermeGear Inc., Hellertown, PA) used is depicted in Figure 1. The cell was used to measure the mass transfer rate of NaCl through SiO_2-water nanofluid embedded within 0.4 μm pores of a track etched polycarbonate membrane. This membrane has a manufacturer reported porosity of 18.8%. Based on the modified form of Renkin's equation [1], the membrane pore size is large enough that the Brownian motion of nanoparticles present in the membrane pores are within approximately 90% With this configuration, the NaCl diffusion path is depicted in Figure 2, diffusion occurs through a liquid film adjacent to the membrane in the high concentration cell, through liquid filled pores of the membrane, and subsequently through the liquid film adjacent to the membrane in the low concentration cell. The diffusion cell is constructed of 6.5 mL glass half cells with 5 mm diameter circular throats on the clamping surfaces that

sandwich the polycarbonate membrane. The half cells are mixed using 7 mm discs magnetically stirred at 600 rpm as verified with digital stroboscope (Ametek, Largo, FL, 1956) over the range of volume fractions studied. In order to obtain liquid tight sealing between the two half cells, petroleum jelly was added to edge of clamping surface between the cells. Each half cell contained two circular ports on the top of the diffusion cell; one 15 mm diameter opening for inserting the 13 mm chloride ISE and one 7 mm opening for fluid addition and sampling. Paraffin film (Thermo Fisher Scientific Inc., Pittsburgh, PA, 13-374-10) was used to seal sample ports and fitted probes to prevent the evaporation losses during mass transfer studies.

The mass transfer rate of NaCl across the membrane in the diffusion cell was evaluated by monitoring the change rate of chloride concentration in each half cell. Initial concentrations were at approximately 3000 ppm and 100 ppm in the high and low concentration half cells, respectively. To observe large concentration differences in both half cells, the concentrations were monitored using chloride ISEs over 9 hours with data stored using a bench top multi-parameter meter (Thermo Fisher Scientific Inc., Pittsburgh, PA, 13-642-055). The mass transfer rate is transient as the concentrations change over time, but the transfer parameters are constant and can be determined experimentally. The overall NaCl mass transfer resistance (RT) can be calculated using equation 1.

$$\ln \frac{\Delta C_t}{\Delta C_0} = -\frac{2A_p}{vR_T} t \tag{1}$$

where A_p is the pore area of the membrane (3.7 mm^2), v is the total volume of solution (5.2 mL), ΔC_0 and ΔC_t represent concentration differences between cells at initial and at measurement time t, respectively. R_T is the total mass transfer resistance provided by the membrane (the first term on the right hand side of equation 2) and adjacent liquid film layers (R_b) on each side of the membrane [2].

$$R_T = \frac{\delta_m}{D_{NaCl} n_p \pi (\frac{d_m}{2})^2} + 2R_b \tag{2}$$

where δ_m is thickness of membrane (25 μm), D_{NaCl} is NaCl mass diffusivity at temperature 25 ºC , 1.6×10^{-9} m^2/s is taken from [3], d_m is membrane pore diameter (0.4 μm), n_p is pore density of 1.5×108 pores/cm^2, and 13.76 min/cm is calculated for membrane resistance.
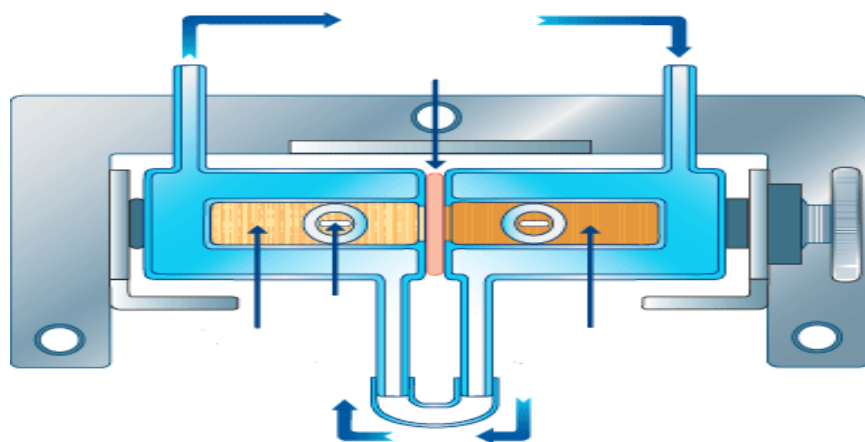
Figure 1 – Membrane diffusion cell configuration viewed from above, used with permission (PermeGear Inc., Hellertown, PA).
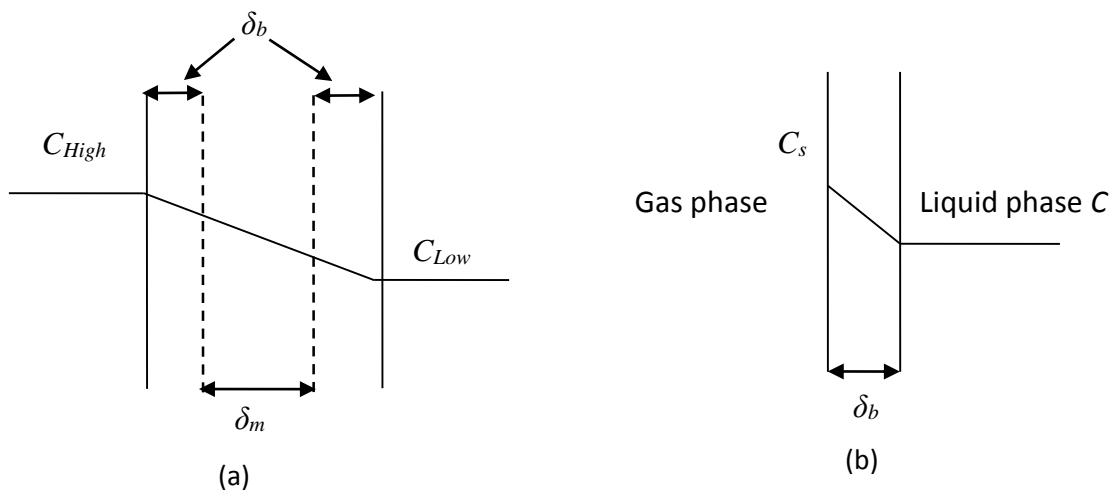

(a)

(b)

Figure 2 – (a) Resistance to NaCl mass transfer. Transfer occurs from the high concentration cell (C_{High}) to the low concentration cell (C_{Low}) with passage through one liquid boundary layer of thickness of δ_b, a membrane of thickness δ_m and another liquid boundary layer of thickness δ_b. (b) Resistance to oxygen mass transfer. Transfer occurs from the gas phase at a saturated oxygen concentration C_s to liquid phase at an oxygen concentration C through a liquid boundary layer of thickness δ_b.

R_T is determined from the line of best fit slope when plotting $\ln(\Delta C_0/\Delta C_t)$ versus time and was determined in triplicate for nanoparticle concentrations of 0.5, 2.5 and 5 vol % at 25 oC. The chloride ISEs used had manufacturer reported reproducibility of 2% and half-cell mass balances

6

agreed within 2%. To account for potential interference of nanoparticles on probe readings, prior to the start of each measurement, the probes were calibrated in standard NaCl solutions that included equivalent nanoparticle concentrations used during the mass transfer measurements.

The oxygen mass transfer measurements did not involve transport through the membrane. Only half of the diffusion cell was used. The membrane was removed and the cell throat sealed with paraffin film. The same stirring arrangement described previously was used. Oxygen exchange from the atmosphere occurred at the air-nanofluid interface through the two ports of the half cell. As depicted in Figure 2, the diffusion path incorporates only the liquid film at the air-nanofluid interface. The half-cell probe port was fitted with a 12 mm diameter oxygen selective electrode (Hach, Loveland, CO, 5197000), calibrated daily according to manufacturer recommendations. For these oxygen transfer studies, nanopure water was deoxygenated with 1 g/L sodium sulfite and 1 mg/L $CoCl_2$ added to the cell.

For the oxygen transfer experiments, a volumetric mass transfer coefficient (K_La) (equation 3), is calculated based on the oxygen concentration change rate, with initial dissolved oxygen concentration C_0, saturated dissolved oxygen concentration C_s, and dissolved oxygen concentration when time is t, C_t.

$$\ln(\frac{C_s - C_0}{C_s - C_t}) = K_L a t \tag{3}$$

C_S is influenced by environmental conditions of barometric pressure and temperature. To account for slight variations in these conditions, C_S was determined for controls and individually for each treatment as the average C_t over a 20 minutes duration once C_t ceased to continuously increase for each nanoparticle volume fraction studied. K_La was determined in triplicate for nanoparticles of 20.0 ± 1.1 nm and 24.5 ± 2.4 nm at concentrations of 0.5, 2.5 and 5 vol % at 23 ± 2 °C.

1.1.4. Viscosity and Density Measurements

Interfacial mass transfer resistances vary with solution viscosities. In this study, viscosities of nanofluids comprised of a base fluid containing 1 g/L sodium sulfite and 1 mg/L $CoCl_2$ and 0, 0.5, 2.5 and 5% volume fraction SiO_2 nanoparticles were measured using a falling ball viscometer (Cole-Parmer, Vernon Hills, IL, WU-08701-00) at room temperature (23.5 ± 1 °C). Densities were determined from mass measurements using an analytical balance (Thermo Fisher Scientific Inc., Pittsburgh, PA, 01-920-051) for pipetted (Thermo Fisher Scientific Inc., Pittsburgh, PA, 05-403-121) sample volumes from 1-5 mL. Three replicates were conducted for each sample. Measurement procedures were verified with nanopure water. Nanopure water dynamic viscosity was measured at 0.958 mPa·s; in close agreement with the literature reference value of 0.97 mPa·s [4]. Measured nanopure water density was 998 kg/m^3, close to the reference value of 997 kg/m^3 at 23.5 °C [5].

1.2. Results and Discussion

1.2.1. Adsorption

Measured chloride concentrations before and after 50 hours incubation are did not change and results in this study are interpreted for conditions of mass transfer without physical adsorption.

1.2.2. Viscosity and Density

Shown in Figure 3 are nanofluid dynamic viscosity and density. The density and viscosity increase with increasing SiO$_2$ volume fraction. The viscosity of 5% nanofluid is 1.3 mPa·s. This is 47% higher than that of the base fluid containing no nanoparticles. The well-known Einstein correlation [6] can be used to predict solution viscosities of particle suspensions when volume concentration is less than approximately 5%. Using the Einstein correlation, the predicted 5% nanofluid viscosity is 1.0 mPa·s, 30% less than the measured value. Failure of the Einstein correlation to predict nanofluid viscosities were reported elsewhere [7, 8]. Our measured viscosity value is similar to that of Nguyen et al [8] . (2007a) for a 5% 36 nm Al$_2$O$_3$ nanofluid who measured a viscosity of 1.5 mPa s at ambient conditions.
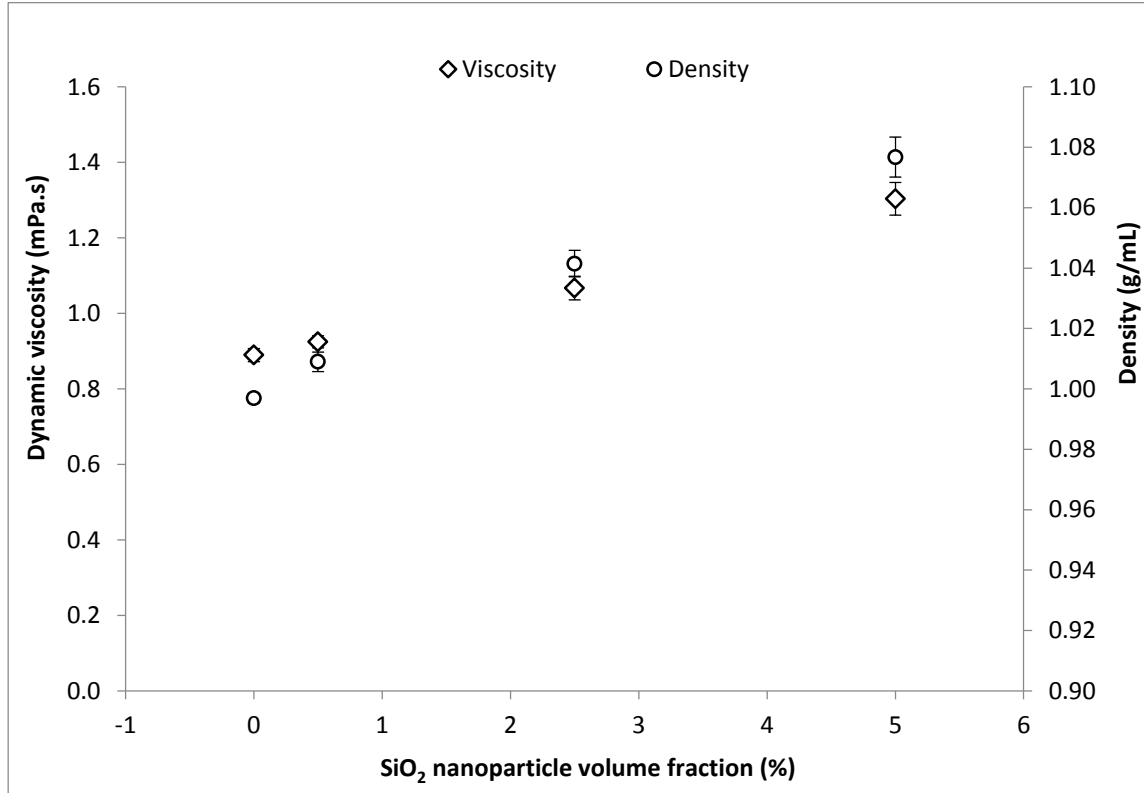

Figure 3 – Dynamic viscosity and density of 0, 0.5, 2.5 and 5% volume fraction SiO$_2$ nanofluids.

1.2.3. Nanoparticle Effects on Oxygen Transfer

Shown in Figure 4 are oxygen volumetric mass transfer coefficients (K_La) for different volume fractions, and two different nanoparticles sizes. Nanoparticle diameters used are within 5 nm difference, and an effect of nanoparticle sizes on K_La is not apparent in Figure 4. Thus, when comparing volume fraction effect, an average K_La of both sizes is used for the same volume fraction. The average K_La for the controls, 0.5% and 2.5% are not significantly different. The 5% volume fraction K_La is significantly lower than the control with a 33% reduction.

Reduced mass transfer rates found in this study may be attributed to both an obstruction effect of impermeable nanoparticles and also to nanoparticles increasing solution viscosities. The obstruction effect of nanoparticles on oxygen diffusion within a liquid film can be estimated using

8

the Maxwell equation [9] where the oxygen impermeable nanoparticles can elongate oxygen transfer pathways.

$$\frac{D_{eff}}{D} = \frac{1-\phi}{1+\phi/2} \qquad (4)$$

where D_{eff} is the effective diffusivity with presence of nanoparticles, D is the diffusivity in solution without nanoparticles.
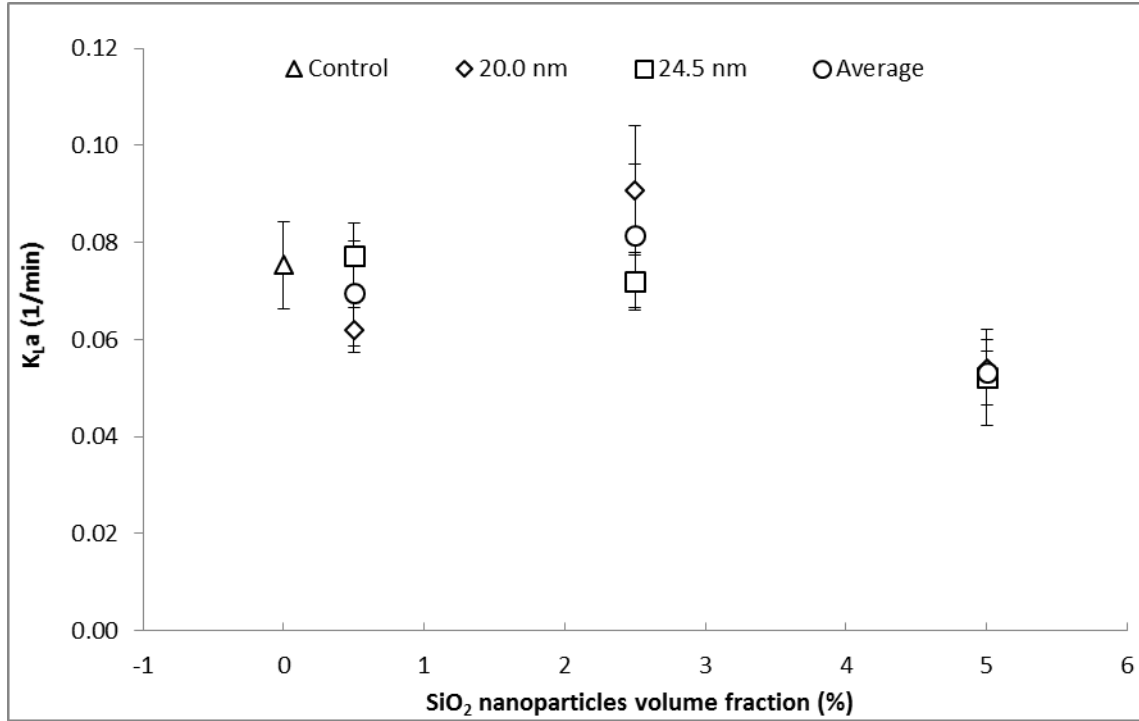

Figure 4 – Oxygen volumetric mass transfer coefficient (K_La) of nanoparticle free control and 0.5, 2.5 and 5% volume fraction SiO$_2$ nanofluids for 20.0 nm, 24.5 nm nanoparticles and average of two different sizes.

Using equation 4, the obstruction effect predicted provides a 7.3% reduction for 5% volume fraction nanoparticles, which cannot account for the 33% reduction in this study. However, nanoparticles influence solution viscosity and liquid film mass transfer coefficients are known to decrease with viscosity increases. In this study, viscosity effects can be estimated using equation 5 [10], a dimensionless correlation for predicting liquid film mass transfer coefficients in a similar horizontal diffusion cell and stirring configuration.

$$Sh = 0.0157\,Re^{1.03}\,Sc^{1/3} \qquad (5)$$

where $Sh = K_L d/D$, $Re = V d_s \rho/\mu$, $Sc = \mu/\rho D$, K_L is the liquid film mass transfer coefficient, D is mass diffusivity, d_s is star-head magnetic stir bar diameter, ρ is density of solution, V is velocity, and μ is solution dynamic viscosity. Measured viscosities and densities are shown to increase with nanofluid volume fraction in Figure 3. Using equation 5 with a viscosity of 1.3 mPa s for 5% nanofluids and viscosity of 0.89 mPa·s for the nanoparticle free control provides an estimated 22.4% reduction in the liquid film mass transfer coefficient at 5% volume fraction. This viscosity

effect along with the reduction due to diffusion blockage (equation 4) yields a total 30% decrease of the transfer coefficient and it is close, within experimental uncertainty, to the observed 33% decrease. The slight difference in prediction may also be caused by uncertainties associated with our viscosity measurement method. Regardless, in this study, any mass transfer benefits associated with nanoparticle Brownian motion must be minimal and are overshadowed by detrimental viscosity effects.

1.2.4. Nanoparticle Effects on NaCl Mass Transfer

Shown in Figure 5 are NaCl mass transfer resistances (R_T) for the control and with 0.5 - 5% volume fractions for two different nanoparticle sizes. No consistent nanoparticle size effect is seen. As volume fraction increases, R_T appears to increase slightly or shows no significant change given the experimental uncertainty. The membrane provides the majority of mass transfer resistance for this configuration; and this resistance is independent of viscosity effects. Hence, significant increases in mass transfer resistance due to viscosity effects are likely to be less apparent than those observed during gas absorption measurements.
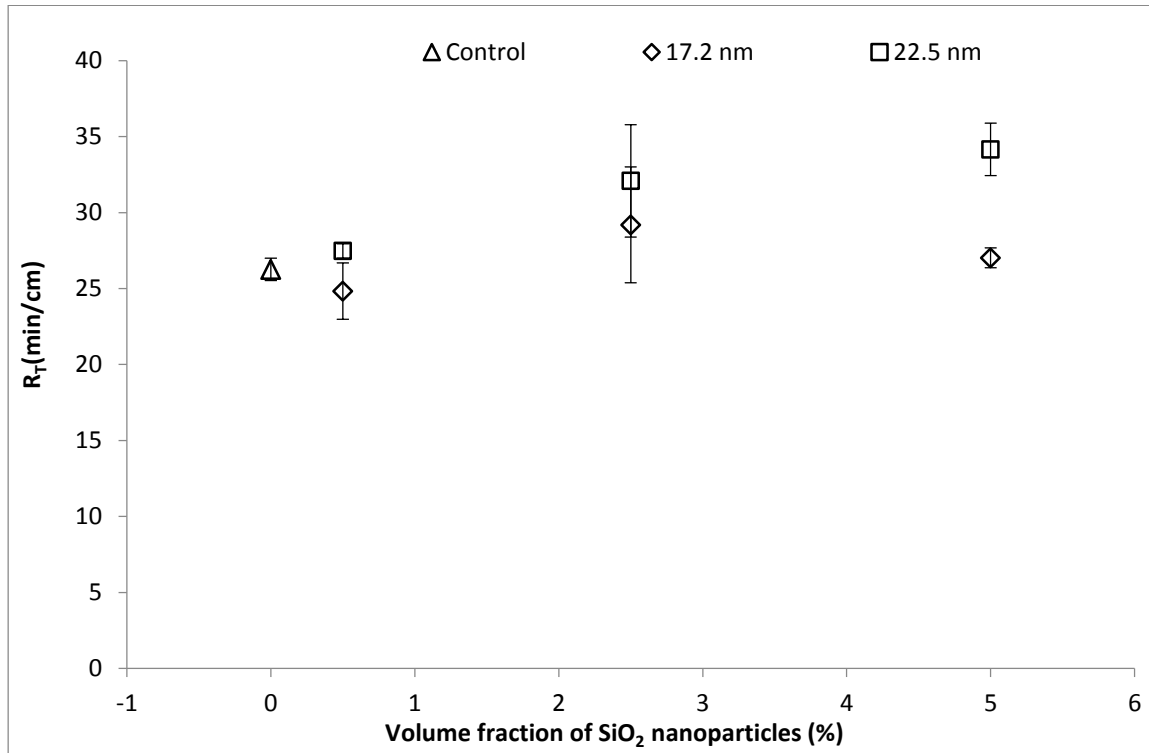

Figure 5 – NaCl mass transfer resistance (R_T) of nanoparticle free control and 0.5, 2.5 and 5% volume fraction SiO_2 nanofluids for 17.2 and 22.5 nm nanoparticles

1.2.5. Interpretation of Results

Findings of no effect or decreased mass transfer rates for nanofluids in our study is contrary to other studies that report enhanced diffusion or mass transfer in nanofluids [11-14]. The reasons for

this discrepancy are unclear. Measurement uncertainty can be dismissed as the cause; the lowest reported mass transfer enhancement 190% [14] and, based upon a first-order second-moment uncertainty analysis [15] our propagated experimental uncertainty is only 6% for the NaCl transfer measurements and only 5% for the oxygen transfer measurements. Particle type may play a role. In this study a silica nanofluid was used and our results are similar to Turanov and Tolmachev [16]who also investigated a silica nanofluid and reported a 25% ^{1}H self-diffusion coefficient reduction at a 23% nanoparticle volume fraction. Why particle type matters is unclear, nanoparticle Brownian motion creating a zone of influence is proposed by others [17, 18]) to explain enhancement results, but this same motion and effect would be expected independent of particle type. Finally, our measurements were for mass transfer in a non-reactive system and herein may be the true difference. Enhanced mass transfer rates have been reported exclusively for mass transfer accompanied and enhanced by chemical reaction. How chemical reaction is accounted for may complicate interpretation of results. Komati and Suresh [17] acknowledge interfacial adsorption could contribute to their measured enhancements for nanofluids. Similarly, Ozturk et al. [19] argue that the anomalous enhancement for diffusivities determined from dye diffusion [12, 20] is due to complexation interactions between the dye and nanoparticles. Complexation reactions result in enhanced mass transfer by creating steep concentration gradients as the diffusing solute is consumed by uncomplexed nanoparticles at the interfacial zone. Measurements in this study were not hampered by interpretation of adsorption and reaction enhancements and thus may provide a clearer understanding of the effects of nanoparticles on mass transfer rates.

1.3. Summary

No mass transfer enhancements were found in the presence of nanoparticles for both of oxygen and NaCl mass transfer. Oxygen transfer was actually diminished at the highest nanoparticle volume fraction; this is attributed the obstruction effect of impermeable nanoparticles and also to solution viscosity effects where increases in viscosity resulted in lower liquid film mass transfer coefficients. These non-enhanced mass transfer results indicate Brownian motion and micro-convection of nanoparticles cannot be the mechanism controlling heat and mass transfer in the nanofluids of this study.

1.3.1 Additional Details of This Study Are Provided in The Following Publications:

Feng, X. and Johnson, D. W. (2012) "Mass Transfer in SiO2 Nanofluids: A Case against Purported Nanoparticle Convection Effects" International Journal of Heat and Mass Transfer Journal, 55, 3447–3453

Feng, X. (2012). Nanoparticle morphology effects in heat and mass transfer processes, The University of Texas at San Antonio.

1.3.2 Details of This Study Were Provided in These Presentations:

Xuemei Feng, Drew Johnson, "Mass Transfer Measurements to Characterize Nanofluid Transport Mechanisms", ASME International Mechanical Engineering Congress & Exposition, Denver, CO, November 11-17, 2011

Drew Johnson, Xuemei Feng, Mass Transfer Measurements to Characterize Nanofluid Transport Mechanisms, United States Air Force Office of Scientific Research Thermal Program review in Arlington, Virginia, September 26-28, 2011

Drew Johnson, Xuemei Feng, *"Characterization of Nanofluid Heat Transfer Enhancements"*, United States Air Force Office of Scientific Research Thermal Program review, Dayton, Ohio, October 13-14, 2010

Xuemei Feng, Drew Johnson, "Characterization of Nanofluid Mass Diffusivity", United States Air Force Office of Scientific Research Thermal Program review, Dayton, Ohio, October 13-14, 2010

Part (2): Are enhancements related to the extent of particle aggregation and morphology of aggregated particles? If so, can the extent of particle aggregation and associated heat transfer enhancements be characterized using fractal dimensions of aggregated nanoparticles?

Heat transfer enhancements, for some nanofluids, may be primarily caused by mechanisms including nanoparticle aggregation forming highly conductive paths. In additional studies, different aggregated morphologies of Al_2O_3 nanoparticle and associated thermal conductivity were investigated. Morphologies were measured with imaging techniques and light scattering methods and quantified using aspect ratios and fractal dimensions. Results showed that highest thermal conductivity enhancement was 29% for 6.4% diffusion limited aggregation (DLA) nanofluids. DLA thermal conductivity enhancements could be predicted with effective medium theory using aspect ratio of 3.65, and the enhancements of dispersed nanoparticle and reaction limited aggregation (RLA) were in agreement with effective medium theory prediction with aspect ratios 1.89 and 1.73.

Effective medium theory incorporating aspect ratio (*a*) to predict the thermal conductivity of mixtures as provided by Fricke [21] is provided in equations 6–10 [22].

$$\frac{k_{NF}}{k_F} = 1 + \frac{ns\phi(\delta_k - 1)}{ns - 1 + \delta_k - \phi(\delta_k - 1)} \tag{6}$$

where ns is a dimensionless shape factor

$$ns = \frac{\beta\delta_k - \beta}{\delta_k - 1 - \beta} \tag{7}$$

with

$$\beta = \frac{1}{3}(\delta_k - 1)[\frac{2}{1 + (\delta_k - 1)L_{11}} + \frac{1}{1 + (\delta_k - 1)L_{33}}] \tag{8}$$

$$L_{11} = \frac{a^2}{2(a^2 - 1)} - \frac{a}{2(a^2 - 1)^{3/2}}\cosh^{-1}(a) \tag{9}$$

12

$$L_{33} = 1 - 2L_{11} \tag{10}$$

where $\delta = k_{NP}/k_F$, and L_{11} and L_{33} are the spheroid depolarization factors of main axis and the direction perpendicular to the main axis, respectively.

2.1. Experimental Methods

2.1.1. Nanofluid Preparation

Al_2O_3 nanoparticles with a nominal size of 50 nm were used in this study (Alfa Aesar, Ward Hill, MA, 12733), size was verified at 54.2 ± 2.0 nm with a polydispersity index of 0.25 ± 0.02 using DLS with a 658 nm laser and a scattering angle of 165° (Beckman Coulter Inc, Brea, CA, Delsa Nano C). The nanoparticles were purchased as a 4.8 vol% (20 wt%) stock solution of pseudo–Boehmite ($Al_2O_3 \cdot H_2O$) at pH 4 in the presence of HNO_3. Nanofluid concentrations before ionic strength adjustment were in the range of 1.2 to 7 vol%. Dilutions of stock solution using nanopure water of resistivity 18.2 MΩ·cm were used to create nanofluid concentrations of 1.2 to 3.3 vol%. Concentrations above 4.8 vol% were obtained by evaporating 12.6 mL of 40 mL stock nanofluids in 40 mL borosilicate glass vials at 100 °C for five hours (Thermo Fisher Scientific Inc., Pittsburgh, PA, Isotemp oven model 630G) to provide a stock nanofluid concentration of 7 vol% that could be further diluted. To mitigate any possible nanofluid aggregation occurring during storage and evaporation processes, before usage, nanofluids were sonicated (Thermo Fisher Scientific Inc., Pittsburgh, PA, FS60H) for at least two hours at 100 W at 42 KHZ. After sonication, sizes were measured to be 51 ± 1 nm with a polydispersity index of 0.24 ± 0.02 using the same technique as described previously for stock nanofluids.

After evaporation and dilution steps, ionic strength adjustments were made by adding appropriate amount of ACS grade NaCl to create DLA and RLA regimes. The concentrations of NaCl necessary for RLA or DLA were determined based upon aggregation kinetics, similar to other studies [23, 24], where aggregation rates were determined by monitoring particle size changes with time. Using DLS, aggregation rates were recorded with time. Conditions studied were at 25 °C for 2 mL nanofluid with different amounts of NaCl added. Nanoparticle aggregation rates increase with nanoparticle concentration. The nanoparticle concentration used for kinetics studies should be low enough; so that sizes change with time can be discerned to follow either a hyperbolic or parabolic trend before particles become large enough to precipitate during DLS monitoring. Hyperbolic aggregation corresponds to a DLA regime and parabolic aggregation indicates RLA behavior [23, 24]. The nanofluid concentration used in this part of study was 1.2×10^{-3} vol%; this is close to detection limit of the DLS instrument, but was necessary to provide aggregation slow enough such that DLA and RLA could be distinguished without precipitation. Trial and error was used to determine the necessary NaCl concentration for DLA and RLA behaviors, and aggregation rates were monitored for nanofluids of 1.2×10^{-3} vol% containing 90–500 mM of NaCl. A critical NaCl concentration was determined as the concentration where additional amounts of NaCl do not increase aggregation rates. RLA transforms into DLA at this critical NaCl concentration.

2.1.2. Thermal Conductivity Measurements

NaCl concentrations above and below the critical concentration were used to create nanofluids with different aggregate morphologies suitable for thermal conductivity measurements. The volume fractions of nanofluid used for thermal conductivity studies were high enough (1.04–6.4 vol%) such that DLA and RLA formed viscous nanofluid gels. Thermal conductivities of DLA, RLA and dispersed nanofluids were measured over 3.5 hours with a KD2 pro thermal properties analyzer (±5% accuracy, Decagon Devices, Inc., Pullman, WA) using the transient hot wire method [25]. Three samples were measured, and each sample was measured 15 times over 3.5 hours. According to the manufacturer, for each measured heat is applied for 30 seconds, and temperatures values are measured over 1 minute. Sixty temperature readings are used to compute thermal conductivities. Temperature rise was observed less than 0.6 $^{\circ}$C. To dissipate the thermal gradient, a 15 minute interval was used between each thermal conductivity measurement. To perform these measurements, nanofluids along with appropriate amounts of NaCl solution were pipetted (Thermo Fisher Scientific Inc., Pittsburgh, PA, 05-403-121) into a 15 mL graduated polypropylene centrifuge tube (Thermo Fisher Scientific Inc., Pittsburgh, PA, 12-565-286B) creating a total volume of 16.7 mL of mixture that excluded any head space when the tube was caped. The probe of KD2 pro analyzer was then inserted into the nanofluid through a hole drilled into the cap and fixed with tape (Thermo Fisher Scientific Inc., Pittsburgh, PA, 15-901-10G). The tube was placed in a plastic rack (Thermo Fisher Scientific Inc., Pittsburgh, PA, 5970-0213), housed in an incubator free of room interference, and the thermal conductivities of nanofluid measured at 25 $^{\circ}$C. The measurement accuracy was verified using nanopure water, with a resistivity of 18.2 MΩ·cm, and glycerol provided from the manufacturer. Thermal conductivity of measured values for water and glycerol were at 0.581±0.004, 0.280±0.001 W/m·K, respectively. Compared to literature reported values of 0.609 ± 0.003 W/m·K [26] and 0.285 W/m·K [27], our measurements were within 5% uncertainty of the analyzer. Similar discrepancies have been reported in other studies [28]. Nonetheless, to minimize potential measurement biases, results are interpreted as a thermal conductivity ratio of nanofluid to the associated base fluid. Additions of NaCl are known to decrease water thermal conductivities [29]. Thus, base fluid thermal conductivities for DLA and RLA were determined by measuring thermal conductivities of nanopure water with appropriate amounts of NaCl added. Thermal conductivities of DLA and RLA base fluids were measured at 0.570 ± 0.007 W/m·K and 0.582 ± 0.005 W/m·K, respectively. These values are within 5% of the tabulated values of [29]

2.1.3. Nanoparticle Imaging

Shapes of dispersed nanoparticles were observed with AFM (Bruker AXS, Santa Barbara, CA, MultiMode) under dry conditions. In order to minimize possible aggregation artifacts caused by evaporation processes, Al_2O_3 nanoparticles were diluted to 1.2×10^{-3} vol% prior to imaging. This concentration provided nanoparticles well distributed in the image. Furthermore, enough nanoparticles could be observed to provide adequate shape information while presumably maintaining equivalent aggregation extent present in the fluid sample. To obtain AFM images, 20 μL of diluted nanofluids was pipetted (Thermo Fisher Scientific Inc., Pittsburgh, PA, 05-402-87) onto a clean mica substrate. AFM images were captured in a tapping mode at a scan rate from 0.501–0.698 Hz. AFM was not able to provide accurate three-dimensional images and nanoparticle heights were not representative of actual nanoparticle size when compared with DLS measurements. Hence, instead of using AFM, two-dimensional images of aggregated

14

nanoparticles were obtained using better resolution SEM. Because aggregated nanoparticles are unstable, higher dilution factors, 1.2×10^{-3}–1.2×10^{-5} vol%, were used during SEM sample preparation. Approximately 10 µL of diluted nanofluids were pipetted onto 300 mesh carbon-coated copper grid (Electron Microscopy Sciences, Hatfield, PA, HC300-Cu 300). Samples were air dried for two hours before capturing images with SEM (Hitachi, South San Francisco, CA, S-5500) in a bright field mode at a voltage of 20 to 30 KV.

2.1.4. Aspect Ratio Characterization

Nanoparticles images captured from AFM and SEM were used to analyze aspect ratios. Aspect ratios are calculated as the longest dimension divided by the average short dimension. Dimension measurements were obtained using Nanoscope version 7.30 software for analysis of AFM images, and Gatan DigitalMicrograph for analysis of SEM images.

A second way to quantify aspect ratios is through DLS measurements. The DLS method detects the translational diffusion coefficient, and the Stokes-Einstein equation[30], can be used to calculate the spherical diameter. The Stokes-Einstein equation is sufficient for spherical particles but inaccurate for particles that deviate from the spherical shape. Aspect ratio based upon the translational diffusion coefficient of non-spherical particles, can be calculated from Perrin's formulas, as shown in equations 11–13 [31].

$$\frac{1}{d(\theta)} = \frac{\ln\left(\frac{1+\sqrt{1-(\frac{b}{L})^2}}{b/L}\right)}{L\sqrt{1-(\frac{b}{L})^2}} \qquad \text{Prolate ellipsoids} \qquad (11)$$

$$\frac{1}{d(\theta)} = \frac{\tan^{-1}\sqrt{(\frac{b}{L})^{-2}-1}}{b\sqrt{(\frac{b}{L})^{-2}-1}} \qquad \text{Oblate ellipsoids} \qquad (12)$$

$$d(\theta) = \frac{2L}{\pi} \qquad \text{Thick disks} \qquad (13)$$

where L is the major axis length, b is the short axis length, $1/d(\theta)$ is the slope determined from the plot of $\sin^2(\theta/2)/d(\theta)$ versus $\sin^2(\theta/2)$, $d(\theta)$ is the diameter measured at angles (θ) 15° and 165°, respectively.

Aspect ratio calculations from DLS are representative of large particle population as compared to analyzing SEM and AFM images, where a limited number of nanoparticles can be analyzed [32]. However, the difficulty with estimation of aspect ratio from DLS measurements is that one axis length must be known or assumed, and therefore, this method may be less accurate.

15

2.1.5. Fractal Dimension Measurements

SLS was used to determine fractal dimension of aggregates. Fractal dimension is in the range of 1 to 3, $D_f = 1$ corresponds to a line shape and $D_f = 3$ indicates a sphere shape. The volume fractions of nanofluid used for thermal conductivity studies were high enough, such that DLA and RLA form viscous nanofluid gels, and SLS cannot accurately measure the fractal dimension of gels due to multiple scattering problems[33]. Dilution of gels after 3.5 hours of aggregation was performed to overcome this limitation. To ascertain how dilution influences fractal dimension, fractal dimension was measured for serial diluted nanofluids. Fractal dimension of diluted aggregated nanofluids was characterized with SLS (BI-200SM Goniometer, Brookhaven) and calculated based upon equations 14 and 15 [34]. Fractal dimension D_f is determined in triplicate from the line of best fit slope when plotting ln(I(q)) versus ln(q).

$$I(q) = q^{-D_f} \quad \text{When } R_a > 1/q > R_p \tag{14}$$

$$\text{With } q = \frac{4\pi n}{\lambda} \sin(\frac{\theta}{2}) \tag{15}$$

Where q represents wave vector, n is the index of refraction of water 1.3, and λ is the incident laser beam wavelength 632.8 nm, θ is the scattering angle, R_a and R_p are the aggregates radius of gyration and particle radius, respectively.

Fractal dimension analyses were also conducted using the box counting method for the SEM images, where fractal dimension D_f of nanoparticles can be calculated based on the number of boxes N(r) and box sizes r [35].

$$D_f = \lim_{w \to 0} \frac{\log(N(w))}{\log(1/w)} \tag{16}$$

Images were processed and converted into binary formats using Image J software [36] (Bethesda, Maryland), similar to other studies [37-39]. The fractal dimension was determined from the slope of log (number of box) versus log (box size) with box value of 2, 3, 4, 6, 8, 12, 16, 32, and 64 in the algorithm.

2.2. Results and Discussion

Aggregation kinetics of nanofluids, thermal conductivities of different morphologies, diameter and SEM images of aggregated nanofluids, fractal dimension and aspect ratios are presented in this section.

2.2.1. Aggregation Kinetics of Nanofluids

Shown in Figure 6 are the size change with time for 0.0012 vol% Al_2O_3 in 90, 200, 350, 450 and 500 mM NaCl; this information was used to determine the critical NaCl concentration for the transition from RLA to DLA regimes. The characteristic hyperbolic aggregation curve was observed when NaCl concentration was above 350 mM. There was no further increase of aggregation rates when NaCl concentration was above 450 mM, indicating 450 mM NaCl is the

16

critical concentration. The DLA regime occurred when NaCl concentration was higher than this critical concentration. The characteristic parabolic aggregation curve was observed when NaCl concentration was below 200 mM. Based upon these findings, to ensure both regimes were maintained, 500 mM and 90 mM NaCl concentration were used to promote DLA and RLA, respectively.
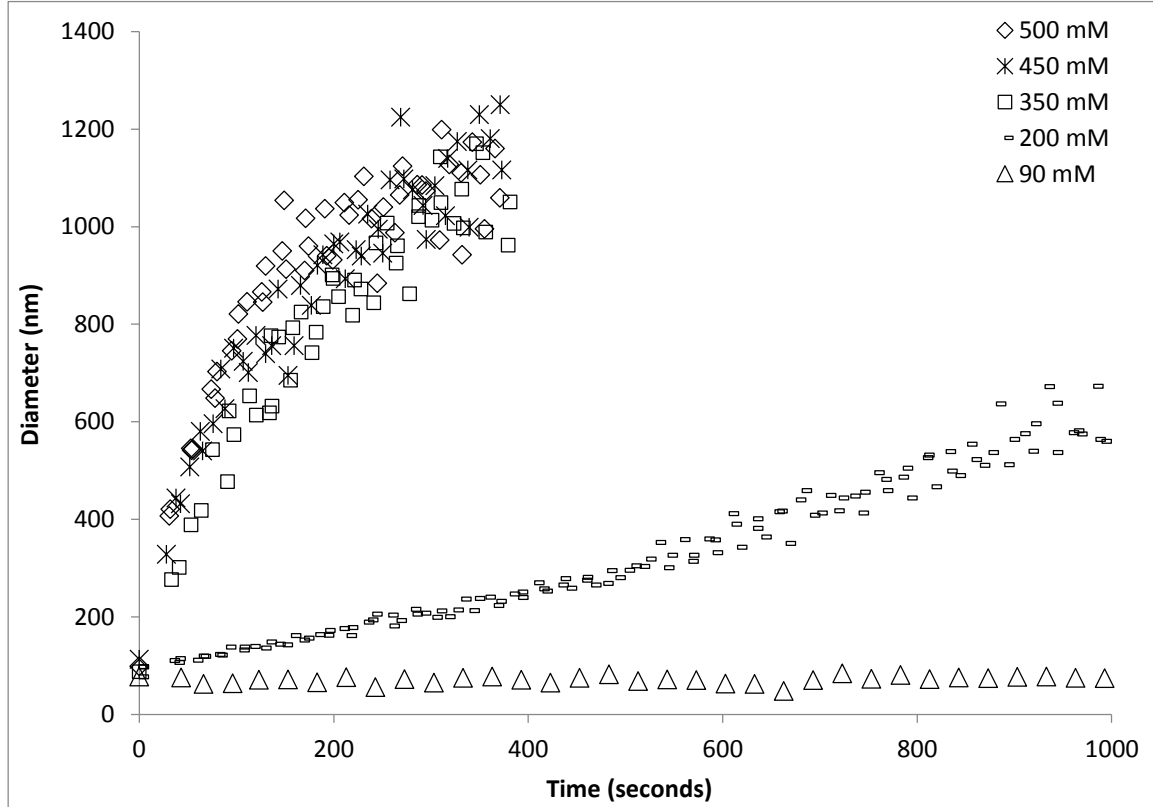

Figure 6 – Aggregation kinetics of 0.0012 vol% in 90, 200, 350, 450 and 500 mM NaCl

2.2.2. Thermal Conductivity Comparisons

Shown in Figure 7 are thermal conductivity ratios of nanofluid to base fluid for: dispersed nanofluid, DLA nanofluid, RLA nanofluid, and predictions from the Maxwell lower bound over a 1.04–6.4 vol% nanofluid concentration range. Thermal conductivity ratios increased with increasing nanofluid concentrations for all types of nanofluid. Predictions from the Maxwell lower bound showed good agreement for dispersed nanofluid concentration below 3 vol%, but the Maxwell lower bound under predicted thermal conductivity ratios for concentrations above 3 vol%. There was no significant difference between thermal conductivity ratios of RLA and dispersed nanofluids. DLA nanofluids showed higher thermal conductivity ratios compared to that of RLA and dispersed nanofluids. The distinct underestimation of the Maxwell lower bound, apparent at high nanofluid concentration for dispersed and RLA nanofluids may be attributed to aspect ratio effects. The aspect ratios of dispersed nanofluids were characterized through AFM and DLS.
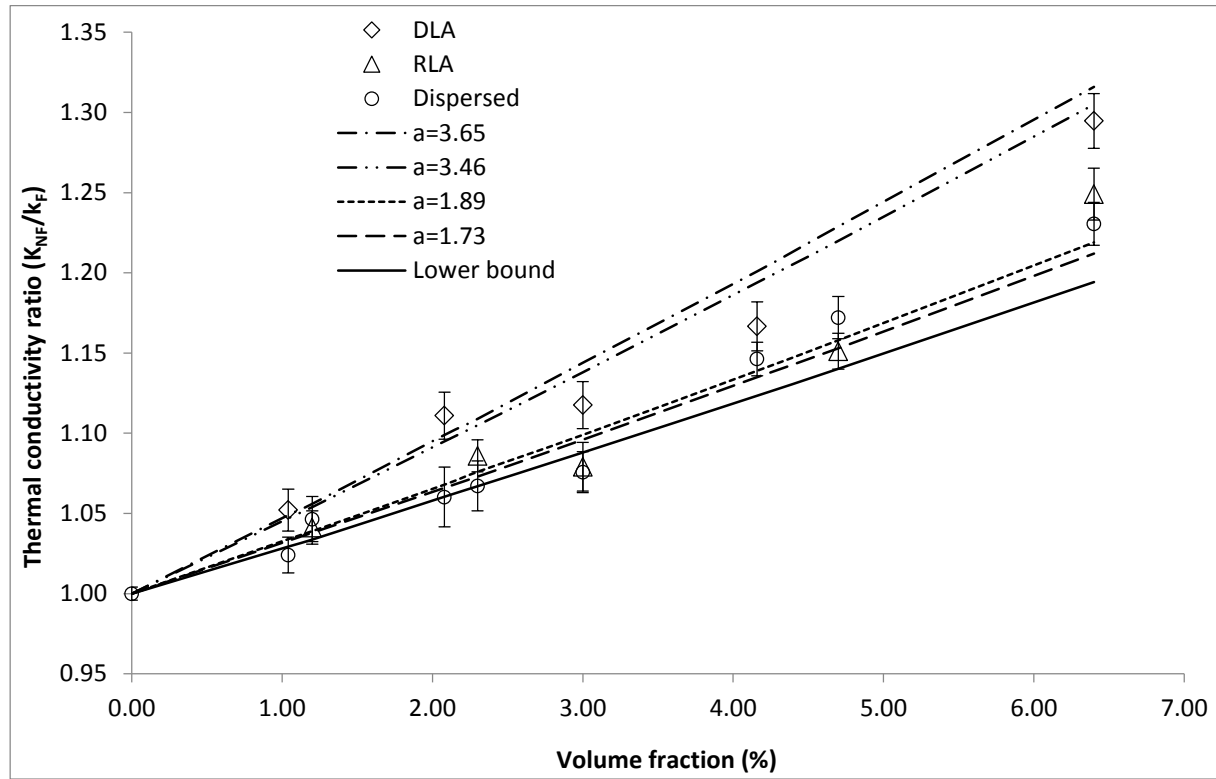
17

Figure 7 – Comparisons of thermal conductivity ratio (k_{NF}/k_F) of dispersed nanofluids, diffusion limited aggregation (DLA) nanofluids, reaction limited aggregation (RLA) nanofluids, the Maxwell lower bound prediction, and Fricke's model with aspect ratios of 1.73, 1.89, and 3.46 and 3.65

2.2.3. Thermal Conductivity Predictions

Shown in Figure 8 is an AFM image used to analyze the aspect ratio of dispersed nanoparticles. Aspect ratio of 1.73 ± 0.60 was found with a major axis length of 71.2 ± 25.3 nm and a minor axis length of 44.9 ± 17.1 nm. Observed sizes were close to the 54.2 ± 2.0 nm, measured from DLS. Samples are considered mono-disperse only if the polydispersity index is below 0.05 [40] and a large variance in aspect ratio was expected for this sample where a polydispersity index of 0.25 ± 0.02 was measured from DLS. Additional DLS measurements were used as an alternative way to quantify aspect ratios. To calculate aspect ratio from DLS information, at least one axis length must be known. Dispersed nanoparticle shape was assumed to be either that of thick disks or oblate ellipsoids. Based upon the AFM image shown in Figure 8, a long axial length was estimated to be 71.2 nm for oblate ellipsoids, and short axis length was estimated to be 44.9 nm for thick disks. This information, along with diameters of 75.9 ± 5.7 nm and 54.2 ± 2.0 nm, obtained at measurement angles of 15º and 165º, respectively, were used in equations 12 and 13 to calculate an aspect ratio of 3.46 for oblate ellipsoids and 1.89 for thick disks. These aspect ratio estimations were then used in equations 6-10 to predict the thermal conductivity ratios, as shown in Figure . The thermal conductivity prediction was higher for Fricke's model with aspect ratio considered

18

than that of the Maxwell model. The highest prediction for dispersed nanofluids was obtained from the aspect ratio of 3.46 from DLS for oblate ellipsoids. Thermal conductivity predictions, using 1.73 from AFM and 1.89 from DLS for thick disks, were in good agreement with measured dispersed nanofluids thermal conductivity. However, it was difficult to conclude based upon inspection of AFM images that dispersed nanofluid shows a homogenous disk shape.
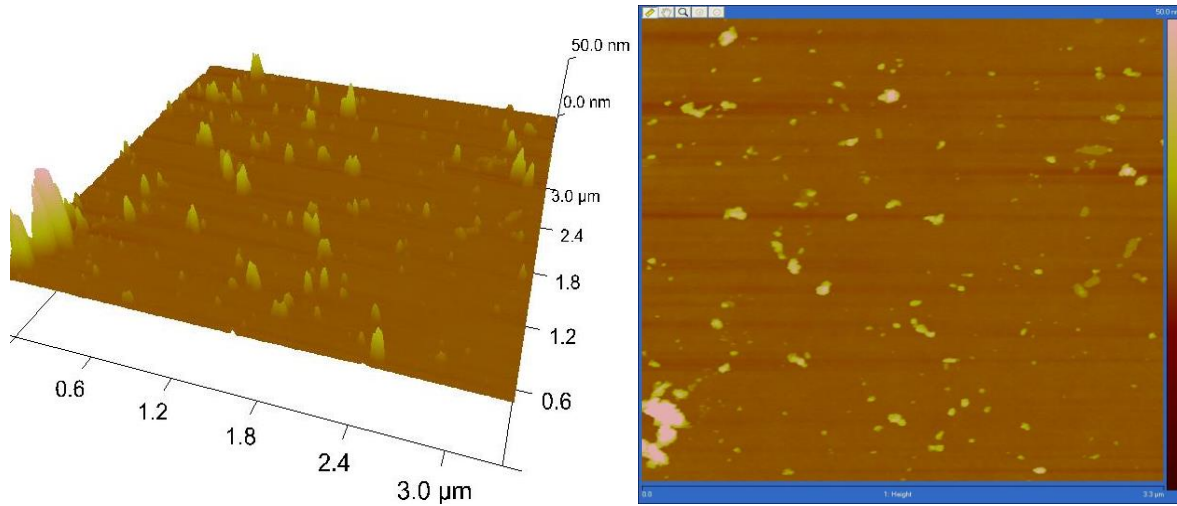

Figure 8 – AFM image of diluted nanofluids at 1.2×10^{-3} vol% after air drying; individual bright nanoparticles can be observed as disks or oblate ellipsoid shapes.

The thermal conductivity ratio of RLA nanofluid was not significantly different from that of dispersed nanofluid. This indicates that the aspect ratio of RLA nanofluids may be close to that of dispersed nanofluids. The thermal conductivity ratio of DLA was greater than that of RLA; this may be caused by aspect ratio differences between DLA and RLA nanofluids. To study shape difference between DLA and RLA, fractal dimensions of DLA and RLA were measured for diluted nanofluids. Fractal dimension of DLA and RLA were averaged over 1.2×10^{-3}-1.2×10^{-5} vol% for comparisons, and yielded an average of 1.81 ± 0.07 for DLA and 2.05 ± 0.04 for RLA, corresponding to loosely linear shape (Df ≈1.8) and a compact shape (Df ≈ 2.1) [41, 42].

Further confirmation of morphology differences between DLA and RLA nanofluids. DLA and RLA nanofluids were observed with SEM. Shown in Figure 9 are the SEM images of 1.2 vol% DLA and RLA nanofluids after being diluted by a factor of 1000. The DLA nanofluids image showed larger clusters compared to that of RLA, which is expected based upon size measurements shown Figure 9. Observed sizes in DLA SEM images agreed with the measurements from DLS. Observed sizes in RLA SEM images appeared much larger than the measurements from DLS, indicating aggregation was occurring during the sample preparation. Thus, further shape analysis of RLA nanofluids was not attempted. Fractal dimension analysis based upon the images of DLA nanofluid was conducted with the box counting method and found to be 1.81 ± 0.11, the same as measured from SLS. This suggests that SEM images can be used to estimate the aspect ratio. Twenty-six aggregated particles were analyzed in 10 images from 3 nanofluid samples and an aspect ratio of 3.6 ± 1.1 was calculated. For comparison purposes, the DLA nanofluid aspect ratio

19

was also determined from DLS measurements. Diameters of 964.4 ± 93.0 nm and 1545.2 ± 60.5 nm were measured at 15° and 165° angles, respectively. Based upon either a long axis of 2100 nm or short axis length of 530 nm from Figure 8, equations 11-13 were used to calculate an oblate ellipsoid aspect ratio of 3.65, a prolate ellipsoid aspect ratio of 1.61, and a disk shaped aspect ratio of 4.63. The best aspect ratio agreement between calculations and images (aspect ratio of 3.6) occurred for oblate ellipsoid shape; though it is difficult to conclude the two dimensional SEM image is representative of a three dimensional oblate ellipsoid shape. Using the aspect ratio of 3.65, equations 6-10, can be used to predict the higher thermal conductivity ratio of DLA nanofluids as shown in Figure 7. This aspect ratio showed reasonable agreement with the highest measured thermal conductivity ratios of DLA nanofluids but tends to slightly over estimate the majority of measured thermal conductivities. This may be attributed to uncertainties associated with the aspect ratio estimation.
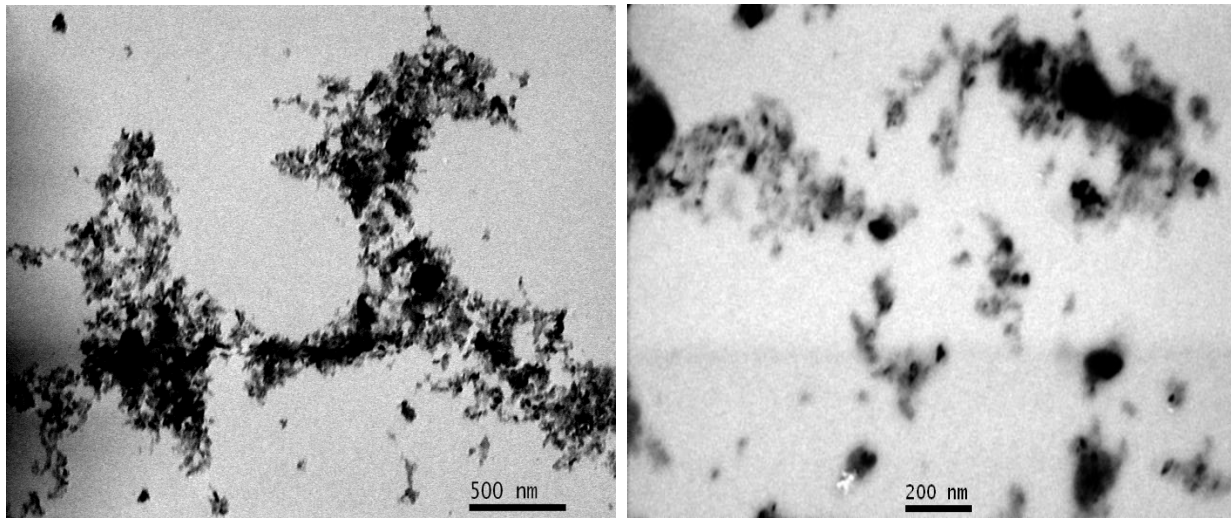

Figure 9 – SEM image of 1.2 vol% Al_2O_3 nanofluids formed under DLA (left) and RLA (right) and then diluted by a factor of 1000

Aspect ratio was calculated based upon the assumption of a homogenous nanofluid; whereas a non-homogenous solution was shown in Figure 9 and not all nanoparticles were shown to be aggregated to the same extent. The largest thermal conductivity enhancement in Figure 7 is 29% at 6.4 vol%. In other aggregations studies [43-46], similar enhancements were observed. Our measured enhancements can be predicted using the aspect ratio of 3.65 for DLA nanofluids. This aspect ratio is comparable to that estimated by Gao et al. [43] who made predictions of thermal conductivity using aspect ratios of as high as 5 based upon TEM images. Comparison of our aspect ratio to other studies shown is not possible as enhancements observed in these studies were simply attributed to aggregation effects without further quantification other than viscosity measurements [43, 46].

Broader comparison of enhancement for Al_2O_3 nanofluid found in this study to other studies that did not focus upon aggregation can also be considered. Nanofluid data shown in Figure 7 have enhancement at 1 vol% of 2.4% for suspended nanofluid and enhancement of 5% for DLA

nanofluid. The benchmark study [28] reported enhancement of 3.6% at 1 vol% for Al_2O_3 nanorods in water. Hence our data is in reasonable agreement with the benchmark dataset for this limited comparison.

2.3. Summary

Nanoparticle aggregation effects on nanofluid thermal conductivities were systematically examined using AFM, SEM, SLS and DLS. Aggregation effects of Al_2O_3 nanoparticles were equated with that of aspect ratio, and incorporating the aspect ratios of dispersed and aggregated nanofluids into effective medium theory showed good agreement between predictions and experimental measurements. Results in our study showed that the thermal conductivities of nanofluids in different aggregation extent can be predicted with classical models if nanoparticle or aggregate aspect ratios were known. A significant finding of this study is that aspect ratios of aggregates, when quantified using various methods, can also be used in the same manner as dispersed phases to estimate thermal conductivity using effective media theory.

2.3.1. Details of This Study Are Provided in The Following Publications:

Feng, X. and Johnson, D. W. (2013) "Characterization of Dispersed and Aggregated Al_2O_3 Morphologies for Predicting Nanofluid Thermal Conductivities" Journal of Nanoparticle Research, 13,6 1-11

Feng, X. (2012). Nanoparticle morphology effects in heat and mass transfer processes, The University of Texas at San Antonio.

2.3.2. Details of This Study Were Provided in These Presentations:

Drew Johnson, Xuemei Feng, "Nanoparticle morphology effects in heat and mass transfer processes" Southwest Research Institute, San Antonio, TX, January 8th 2013.

Xuemei Feng, Drew Johnson, "Experimental Investigation of Nanofluid Brownian Motion and Aggregation Effects on Transport Processes", ASME International Mechanical Engineering Congress & Exposition, Denver, CO, November 11-17, 2011

Xuemei Feng, Drew Johnson, "Experimental Investigation of Nanofluid Aggregation Effects on Thermal Conductivities", United States Air Force Office of Scientific Research Thermal Program review, Arlington, Virginia, September 26-28, 2011

Part (3) Aggregated Nanoparticle Morphology Effects on Membrane Filtration.

The morphology characterization techniques developed to study heat transfer mechanisms were extended and employed to quantify nanoparticle morphology effects on nanoparticle filtration behaviors. Results showed that aggregate morphologies impacted filtration behaviors, and nanoparticle rejections close to 1 were possible even when membrane pore sizes greatly exceed nanoparticle size. There was no difference in terms of rejection between different aggregate

structures. However, filtration resistance of compacted aggregates was 43% higher than that of loose aggregates due to the dense fractal structure of cake fouling layer aggregates. Prediction of cake layer fouling resistances ratio was within 7% difference when using fractal dimension measurements of the aggregates.

Aggregate shape is known to affect filtration resistance [47-50] but few studies have been conducted to explore resistances of aggregated nanoparticles in membrane filtration processes. Membrane filtration flux (J) can be modeled using resistance-in-series [51], as shown in equation 17

$$J = \frac{\Delta P}{\mu (R_m + R_c)} \tag{17}$$

Where ΔP is trans-membrane pressure (TMP), μ is the permeate viscosity, R_m is the intrinsic clean membrane resistance, R_c is the cake layer resistance formed by the deposition of particles on the membrane surface.

Cake layer resistance can be modeled as shown in equation 18 using the Carman-Kozeny model, equation 19 [47]. The cake layer resistance depends upon the cake layer porosity (ε) [48, 50]. Aggregate porosity can be expressed in terms of fractal dimension, D_f, aggregate diameter, d_a, and diameter of primary particles, d_p, within the aggregate as shown in equation 20 [48, 50].

$$R_c = \frac{M}{A_m} \alpha_c \tag{18}$$

$$\alpha_c = \frac{S_s^2 \times K}{\rho_p} \left(\frac{1-\varepsilon}{\varepsilon^3}\right) \tag{19}$$

$$\varepsilon = 1 - \left(\frac{d_a}{d_p}\right)^{D_f - 3} \tag{20}$$

Where α_c is specific cake resistance, M is cake mass onto the membrane, A_m is membrane area, ρ_p is the particle density, S_s is the specific surface, and K is the empirical Kozeny value.

The Kozeny value depends upon both primary particle shape and aggregate porosity. For spherical primary particle shapes with an aspect ratio of 1, the Kozeny value as function of porosity is expressed in equation 21 [52, 53].

$$K = \frac{1}{2} \frac{\varepsilon^3}{(1-\varepsilon)} \frac{1 + \frac{2}{3}(1-\varepsilon)^{5/3}}{1 - \frac{3}{2}(1-\varepsilon)^{1/3} + \frac{3}{2}(1-\varepsilon)^{5/3} - (1-\varepsilon)^2} \tag{21}$$

Equation 21 is specific for spherical particles. However, Brown [54] and others [55, 56], incorporated aspect ratio effects and showed that aspect ratio Kozeny value differences become insignificant for aggregates at high porosity.

Cake layer specific resistances, as expressed in equation 19, have been found under pressures to collapse and alter aggregate morphologies [57, 58]. The extent that morphology rearrangement affects the cake layer specific resistance depends upon the compressibility index (n_c) and applied pressure, as shown in equation 22 [53].

$$\alpha_{cp} = \alpha_c \times (1 + \Delta P)^{n_c} \tag{22}$$

Where α_{cp} is the specific cake layer resistance at ΔP.

Based upon equations 19 and 20, it can be inferred that specific resistances for nanoparticle aggregates formed under DLA conditions are smaller than those formed during RLA, and large colloids with the same effective aggregates size. However, it is still inconclusive whether equations 19 and 20 can predict aggregated nanoparticles filtration performance and it is necessary to conduct additional nanoparticle filtration studies to address whether aggregated nanoparticles filtration performance is abnormal from that of larger colloids in terms of aggregate porosity, cake layer specific resistance, and predictions of equations 19 and 20.

In this study, filtration behaviors of Al_2O_3 nanoparticles under DLA and RLA regimes are investigated. Filtration resistances are measured and compared to estimates from the Carman-Kozeny model using nanoparticle primary and aggregated sizes, aspect ratio, fractal dimension and compressibility index.

3.1. Experimental Methods
3.1.1. Nanoparticle Characterization

Al_2O_3 was selected for this study. This is a commonly used nanoparticle as an abrasive agent [59]. Al_2O_3 nanoparticles were purchased as a 20 wt% (2.38×10^5 mg/L) stock solution of pseudo-Boehmite ($Al_2O_3 \cdot H_2O$) and with a nominal size of 50 nm (Alfa Aesar, Ward Hill, MA, 12733). The nanoparticle aspect ratio of 1.89 with assumption of disk shape was estimated in our previous studies [60]. Using nanopure water of resistivity 18.2 M$\Omega \cdot$cm, the stock solution was diluted to 60 mg/L to produce a nanoparticle concentration close to that used in toxicity studies [61, 62]. Prior to use, nanoparticles were sonicated for at least 2 hours (Thermo Fisher Scientific Inc., Pittsburgh, PA, FS 60H) at 100 W and 42 KHZ, and size was verified at 78 ± 5 nm with a polydispersity index of 0.25 ± 0.09 using dynamic light scattering (DLS) with a 658 nm laser and a scattering angle of 165° (Beckman Coulter Inc, Brea, CA, Delsa Nano C). Differences between manufacturers provided and measured nanoparticle size may be due to aggregation occurring during long storage times before use and also differences in size measurement technique. Manufacturer reported size was determined using transmission electron microscopy.

3.1.2. Aggregation Kinetic Studies

To create different aggregation regimes, different concentrations of ACS grade NaCl were used to aggregate nanoparticles at different rates. NaCl is a common coagulant chosen when studying

nanoparticle aggregation [24, 63]. High coagulant dosing is necessary to promote the DLA, by using NaCl instead of other common water treatment coagulants such as alum or iron, coagulant saturation conditions and sweep coagulation problems can be avoided [64]. Aggregation rates were recorded as growth of particle size with time using dynamic light scattering (DLS) with a 658 nm laser and a scattering angle of 165°. Aggregation rates were monitored in a 4.5 mL methacrylate cuvette for 2 mL of solution under unstirred conditions at 25 °C. In order to capture early stage aggregation, size was obtained with short measurement accumulation times of 15 to 20 seconds. The aggregation regime transforms from RLA to DLA when aggregation rates show no further increase with increasing NaCl concentration [23, 24, 63]. Trial and error was used to determine the necessary NaCl concentration for DLA and RLA behaviors, and aggregation rates were monitored for coagulant dose between 90 – 1000 mM of NaCl. The critical NaCl concentration was determined from where additional amounts of NaCl did not further increase aggregation rates. RLA transforms into DLA at the critical NaCl concentration. The size growths with increasing NaCl concentration were recorded with time, the growth curve for DLA is hyperbolic trend and RLA is parabolic trend [23, 24].

3.1.3. Fractal Dimension Measurements

To quantify the morphologies of DLA and RLA, fractal dimensions were measured in triplicate during aggregation time of 15 to 30 minutes for RLA and 1 to 15 minutes for DLA using SLS (Brookhaven, Holtsville, NY, BI-200SM) at 25 °C. DLA and RLA regimes were created by pipetting (Thermo Fisher Scientific Inc., Pittsburgh, PA, 05–403–121, 05–402–89) 15 mL dispersed nanoparticle solution along with the necessary amount of NaCl concentration into a 20 mL borosilicate glass scintillation vial (Thermo Fisher Scientific Inc., Pittsburgh, PA, 03-337-14). Scattering intensity were recorded and fractal dimension of DLA and RLA were calculated through the logarithmic plot of I(q) versus q based upon equations 15 and 16.

3.1.4. Unstirred Dead End Filtration System

A PVDF membrane (GVWP, Millipore Corporation, Billerica, MA) with pore size 0.22 μm, was used for Al_2O_3 nanoparticle filtration. This membrane is commonly used to study microfiltration [65-67]. Shown in the Figure 10 are a schematic and photograph of the experimental apparatus used for dead end membrane filtration. Membrane filtration of aggregated nanoparticles was conducted under unstirred conditions such that conditions used in the filtration cell matched those used during the aggregation kinetic studies; enabling aggregate particle size to be known during the filtration process. Membranes were housed in a filter cell (MFS, Durham, NC, UHP 25) providing a total filtrate area of 3.5 cm^2 for 12 mL of solution containing nanoparticles and the appropriate concentration of NaCl to promote either RLA or DLA behavior. The same concentration of NaCl solution was then pumped (Dionex, Sunnyvale, CA, GS50 gradient pump) at a flux rate of 171, 257, 343 and 429 $L·h^{-1}·m^{-2}$ through the filter cell until all nanoparticle aggregates, formed from the initial 12 mL of nanoparticles added to the filter cell, were retained by the membrane filter. Flux rates used were somewhat higher than values typically used, 30 – 170 $L·m^{-2}·h^{-1}$ [67], in membrane drinking water filtration operations but were necessary to explore cake layer compressibility aspects and provide sufficient measurable pressure differences between DLA and RLA regimes. Differential trans-membrane pressure was measured using a pressure transmitter (Cole-Parmer, Vernon Hills, IL, EW-68071-62, accuracy ± 0.25%), connected to a computer for data acquisition.
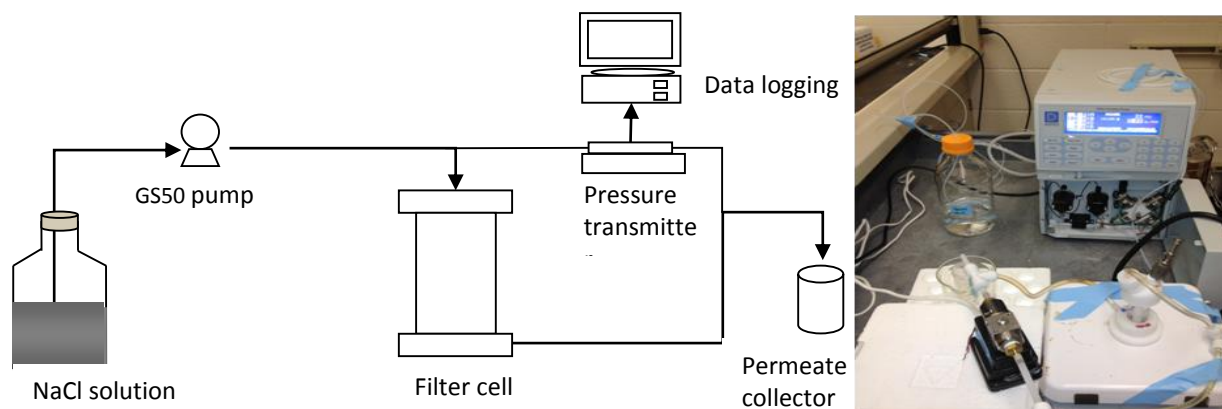
Figure 10. Schematics (left) and photograph (right) of experimental apparatus for membrane filtration using an unstirred filter cell.

3.1.5. Analytical Methods

To determine membrane rejection values, nanoparticle concentrations were measured for initial and permeate solutions using standard calibrated inductively coupled plasma mass spectrometer (ICP-MS) (PerkinElmer, Waltham, MA, USA, DRC-e 9000) or standard calibrated inductively coupled plasma optical emission spectroscopy (ICP-OES) (PerkinElmer, Waltham, MA, USA, Optima 2100 DV). Permeate solutions for both of DLA and RLA regimes were collected over the entire filtration duration. Samples were acid digested before concentration measurements. For acid digestion, 3.2 mL HCl (34–37%, Thermo Fisher Scientific Inc., Pittsburgh, PA, A508-212) and 0.8 mL HNO$_3$ (67–70%, Thermo Fisher Scientific Inc., Pittsburgh, PA, A509-212) were added to 2.5 mL of sample in a 15 mL polyethylene terephthalate centrifuge tube (Thermo Fisher Scientific Inc., Pittsburgh, PA, 05-538-51) and heated at 95 $^{\circ}$C for one hour. For initial samples, the digested solution of was cooled and then diluted by adding 5.5 mL nanopure water (dilution factor of 4.8) and measured directly with ICP-MS. The digested permeate solutions were diluted 48 times through serial dilutions to decrease the acid concentration and measured with higher sensitivity ICP-OES. Removal efficiency was calculated as rejection (R$_j$) based upon the product of the concentration measurements and collected volume (m) equation 23.

$$R_j = (1 - \frac{m_{out}}{m_{in}}) \times 100\% \qquad (23)$$

Where m$_{out}$ and m$_{in}$ are the total nanoparticle mass in permeate and initial solution, respectively.

3.1.6. Membrane Imaging

Unfouled membranes (blanks) and cake layer fouled membranes from the filtration studies were imaged using scanning electron microscopy imaging (SEM). Prior to being imaged, membranes were air dried in the filter cell and residual NaCl crystals were rinsed through the o–ring sealed membrane pores with 5 mL nanopure water. In order to provide conductive surfaces and minimize charging problems during imaging processes, blank and fouled membranes were coated three times with a thin gold film using a sputter coater (Pelco, Clovis, California, SC – 7) at 20 seconds per time. Sputter conditions were at a current of 40 mA and voltage of 115 V. Blank and fouled membranes were cut into slices and fastened onto a sample holder with carbon tape before SEM imaging (Hitachi, South San Francisco, CA, S – 5500) at 6 – 10 KV. Along with imaging, cake layer Al and O element analysis were conducted using energy-dispersive X-ray (EDX) method (Bruker, Billerica, MA, ESPRIT Software).

3.2. Results and Discussion

3.2.1. Kinetic Aggregation

Shown in Figure 11 are the kinetic aggregation studies to determine the critical NaCl concentration necessary to transition from RLA into DLA. Nanoparticle sizes increased with time for all NaCl concentrations used. Parabolic aggregation curve shapes were observed when NaCl concentration was below 200 mM, indicating that RLA regime occurred at concentrations below 200 mM. Hyperbolic aggregation curve shapes were observed when NaCl concentration was above 300 mM. Aggregation rates ceased changing when NaCl concentration increased from 500 mM to 1000 mM, suggesting that the critical NaCl concentration was near 500 mM. In order to compare the filtration resistance of DLA and RLA at equivalent aggregated sizes, filtration of DLA nanoparticles were conducted for approximately 6 minutes after 150 seconds aggregation and RLA were carried out after 1450 seconds (24 minutes) in the same filtration duration. Sizes of particle increased to 900 nm within 150 seconds in 500 mM NaCl, while 1450 seconds passed to reach 900 nm for the 200 mM NaCl solution. The averaged size for RLA filtration processes was 999 ± 101 nm and DLA filtration processes was 1112 ± 101 nm, the aggregated nanoparticle sizes are large enough to be retained by membrane.
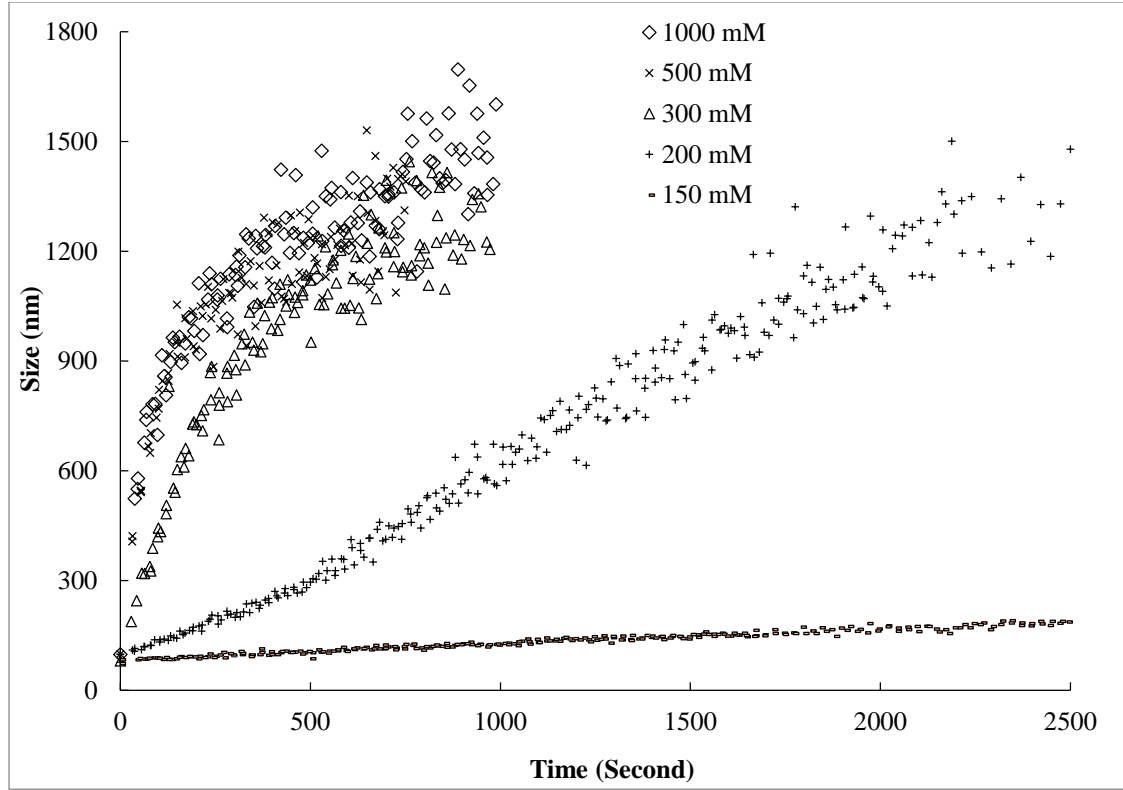
Figure 11. Aggregation kinetics of 60 mg/L Al_2O_3 nanoparticles in 150, 200, 300, 500 and 1000 mM NaCl

3.2.2. Cake Layer Filtration Resistance

Shown in Figure 12 are the TMP for DLA and RLA during the filtration processes, with three replicates for each aggregation regime. The rapid development of TMP over the first 20 seconds of filtration is an artifact associated with the equilibration response time of the pressure transducer when the flow pump was turned on at time zero. The TMP at 20 seconds of filtration is associated with intrinsic membrane resistance and a pressure of 4.5 kPa was recorded. The gradual increases in TMP after 20 seconds of filtration represent the pressure rise caused by formation of a membrane cake layer resistance. TMP continued to increase until the cake fouling layer was fully formed. The TMP of the fully formed cake layer under RLA was 1.43 greater higher than that of DLA as calculated in equation 24.

$$\frac{R_{RLA}}{R_{DLA}} = \frac{P_{RLA} - P_m}{P_{DLA} - P_m} = 1.43 \tag{24}$$

Where TMP of RLA regime (P_{RLA}) is 18.6 kPa, TMP of DLA regime (P_{DLA}) is 14.4 kPa and initial pressure rise (P_m) 4.5 kPa.
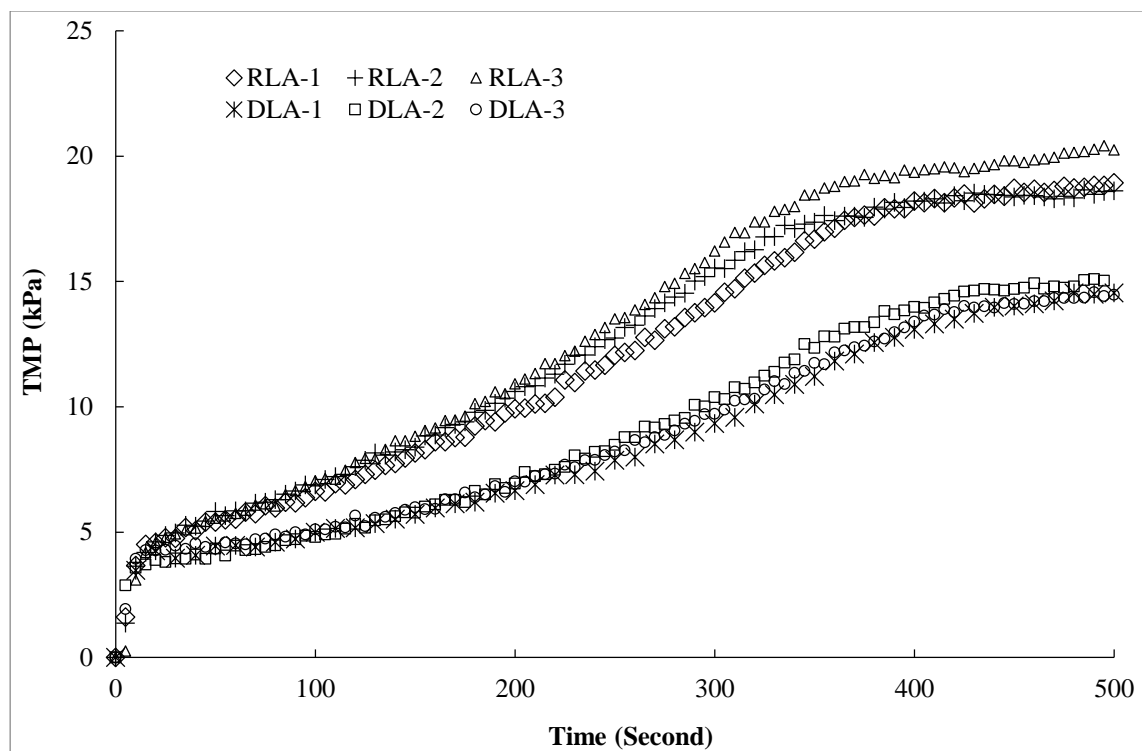
27

Figure 12. TMP of DLA and RLA recorded with time, each aggregation regime was repeated three times

This difference in fully formed cake layer TMP difference could be attributed to differences in membrane rejection or differences associated with the morphologies of the cake layers formed on the membrane surfaces. If membrane rejection was less during DLA filtration than RLA, a lesser amount of cake layer could have formed on the membrane. As was shown in equations 5 and 6, shape differences in DLA and RLA filtration regimes could also lead to the TMP pressure difference. Rejections were calculated based upon measured initial and permeate concentrations, and equation 9 for both of DLA and RLA filtration conditions. Rejection during DLA filtration was 0.98 ± 0.04 and rejection during RLA filtration was 0.99 ± 0.01. Values are not significantly different than 1, indicating that nanoparticles were completely removed using membrane filtration after aggregation for both DLA and RLA. Therefore, it is likely that the TMP difference between DLA and RLA is caused by the differences of aggregate shape.

Membrane cake layers were observed with SEM and analyzed with EDX and images are shown in Figure 13. When compared to the blank membrane, cake layer deposits are easily identified. The surface structure of cake layer formed during filtration with DLA appears to be more porous than that of RLA which shows a dense structure as indicated by the EDX analysis mappings of Al in red dots and O element in green dots. It is important to note that these images represent cake layers after the drying processes necessary for SEM imaging and therefore are not truly representative of the cake layers formed during wet conditions. Nevertheless, they provide a qualitative assessment of the fouling layers formed and suggest cake layer morphology differences are the cause of measured differences in the filtration TMP results.
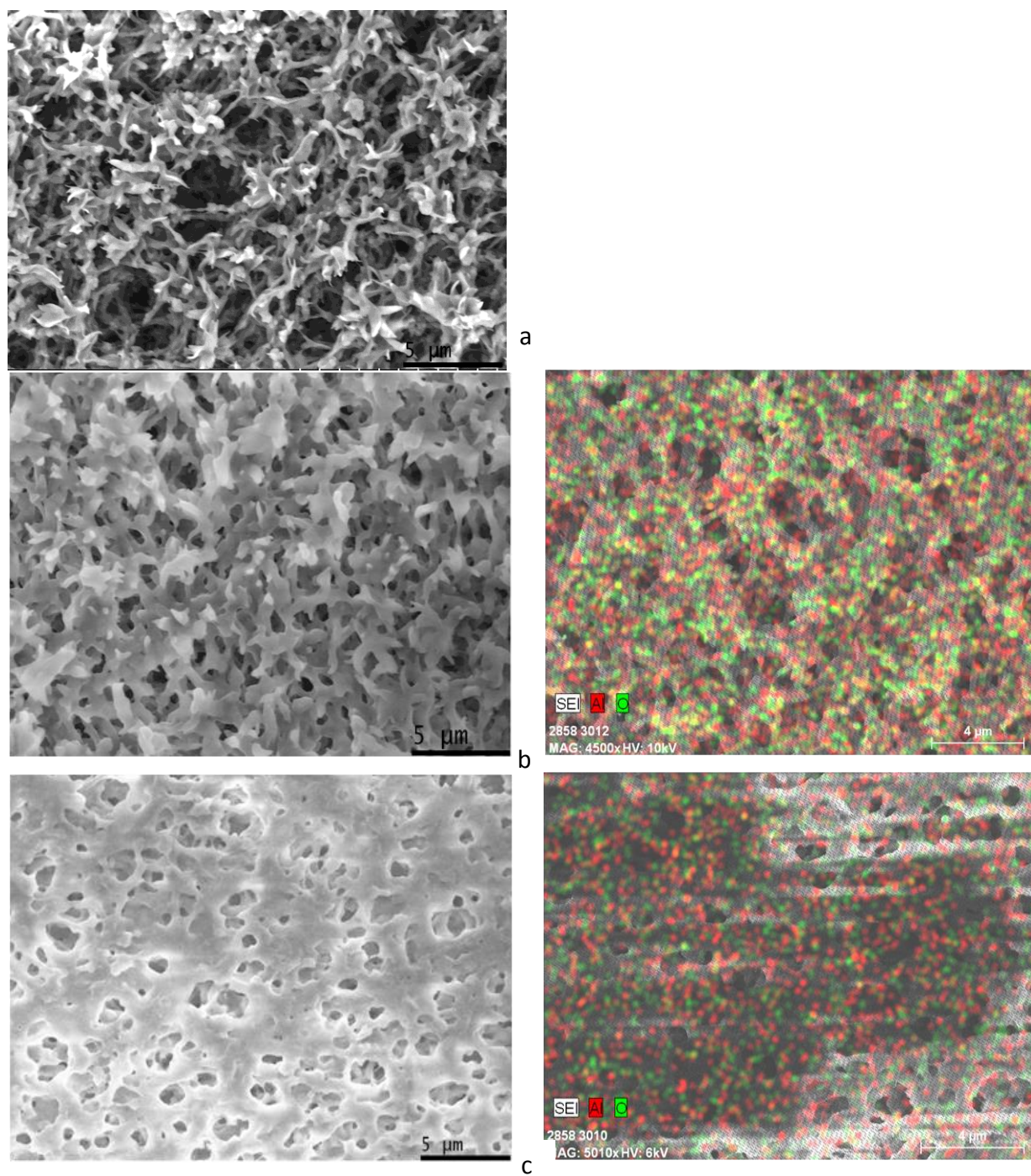
28

Figure 13. SEM images of (a) blank membrane, (b) membrane filtered with DLA nanoparticles (left) and EDX of Al_2O_3 elements mapping (right), (c) membrane filtered with RLA nanoparticles (left) and EDX of Al_2O_3 elements mapping (right). Red dots correspond to Al element, and green dots represent O element

3.2.3　Aggregate Structures

Quantification of aggregate fractal dimension differences between DLA and RLA were further investigated using SLS. Fractal dimension for DLA was 1.39 ± 0.07 and RLA was 1.79 ± 0.08. Fractal dimension were significantly different between the two regimes. A lower fractal dimension indicates a more porous aggregate structure and these values are in agreement with the previous SEM observations. However, the fractal dimensions for both of DLA and RLA measured in this study are smaller than the typical values of 1.8 for DLA and 2.1 for RLA regimes [41, 42]. Our lower fractal dimensions for both of DLA and RLA are unusual, but similar to other studies where salts were used to promote DLA for polystyrene latex resulting in low fractal dimensions of 1.55 [68] or where salts were used to promote RLA for colloidal goethite resulting in a low fractal dimensions of 1.96 [69]. These low fractal dimension are caused by using salts to screen repulsive forces between plate-like particles which in turn promote tip-tip aggregations for both of DLA and RLA regimes [70, 71]. In other words, aggregates evolve not due to contacts between small particles and existing aggregates but rather aggregate to aggregate contacts.

3.2.4　Resistance Predictions and Interpretations

With the measured fractal dimensions of 1.39 for DLA and 1.79 for RLA, the expected specific cake layer resistance ratio ($\alpha_{RLA}/\alpha_{DLA}$) between RLA and DLA can be predicted using equations $19 - 21$ and was found to be 1.37. In this calculation, K is assumed to vary with porosity as shown in equation 21. However, K is also a function of particle aspect ratio [54, 56] and modification of equation 21 was further conducted to take account of this aspect ratio effect. Shown in Figure 14 are how Kozeny values change as a function of porosity for aspect ratios of 2 and 1; also shown is the ratio of Kozeny values for aspect ratios of 2 and 1. Based upon Figure 14 and using an aspect ratio of 2 rather than measured value 1.89 (due to the availability of the existing model data), Kozeny ratios of 1.07 for DLA at predicated porosity of 0.986 and 1.09 at predicated porosity of 0.954 are derived. The specific cake layer resistance ratio for RLA over that of DLA, when accounting for aspect ratios, increases slightly to 1.39. This cake layer resistance ratio is in good agreement with the measured ratio of 1.43 showing only a difference of 3%.

While the cake layer resistance ratio provides an indication of how TMP will change based upon aggregation conditions used, of primary importance is the actual specific resistance values. Based upon equations 17 and 18, measured specific resistances were 5.1×10^{13} m/kg for DLA and 7.3×10^{13} m/kg for RLA. Predicted specific resistance using equations $19 - 21$ were 2.7×10^{12} m/kg for DLA and 3.8×10^{12} m/kg for RLA. Measured values exceeded predicted values by nearly a factor of 19 for both DLA and RLA scenarios. Inaccuracies of specific resistance predictions are often reported [53, 72] and may be attributed to estimates of the Kozeny constant. It is likely that the fractal dimension of aggregates measured free of pressure cannot be used to estimate the porosity of the cake layer with applied pressure due to the compressible nature of cake layers [57, 73].

Compressibility indexes for this study were investigated for both of DLA and RLA. Shown in Figure 15 are the compressibility plots for DLA and RLA cake layers conducted over a flux range of $171 - 429$ L·hr^{-1}·m^{-2}. Compressibility index of 0.72 for RLA and 0.80 for DLA were obtained based upon the linear best fit line slope when plotting the log of α_{cp} versus (1+TMP). The slightly higher compressibility index for DLA is expected since it may be easier to collapse the more porous DLA structures. For comparison, compressibility index between 0 and 1 indicates
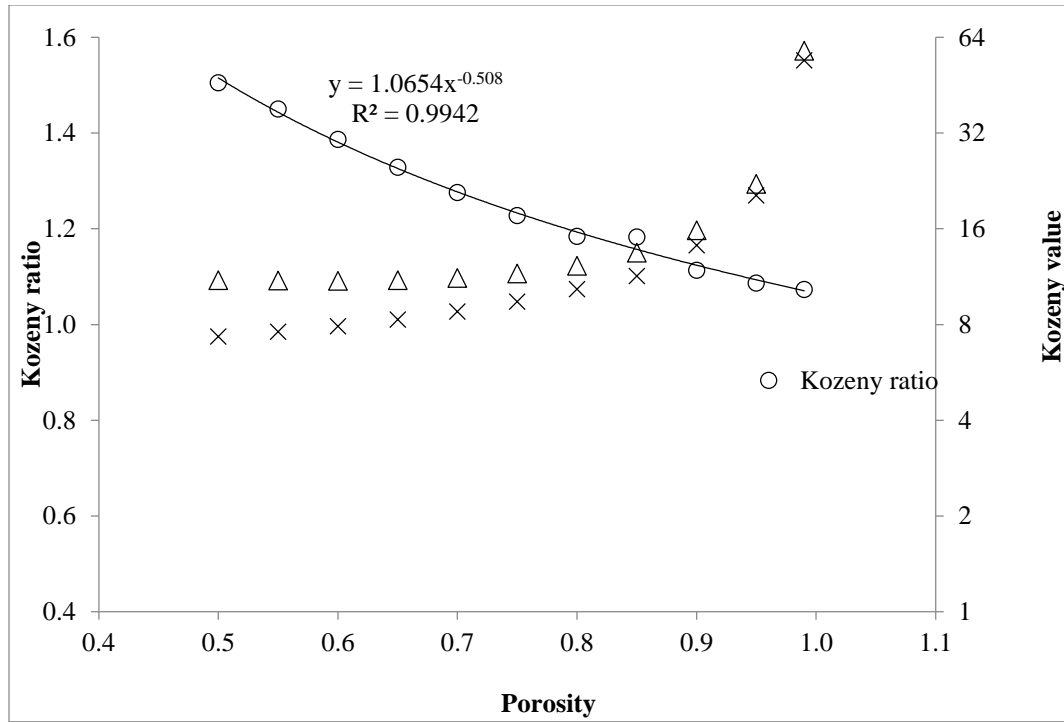
Figure 14. Kozeny values versus porosity (ε) at aspect ratios (a) of 1 and 2. Also shown is the ratio of Kozeny values for aspect ratios of 2 and 1. Data is adapted from [54, 56].

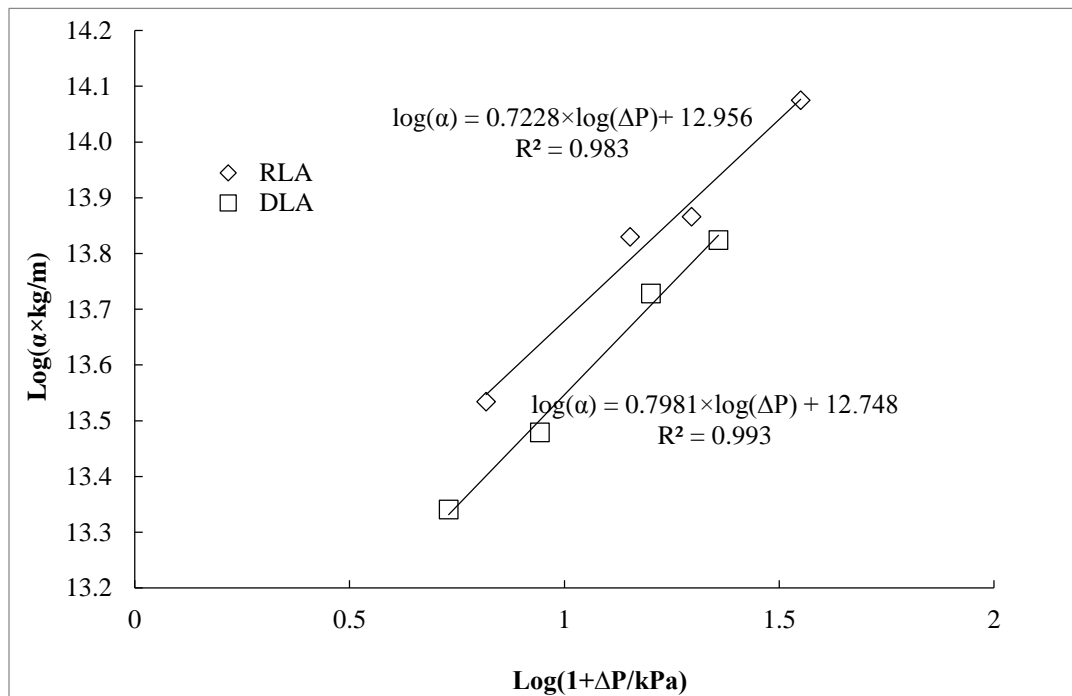Figure 15. Compressibility indexes of DLA and RLA cake layer tested at flux from 171 – 429 L· hr^{-1}·m^{-2}

moderately compressible cake layer [74]. With the measured cake layer compressibility indexes for DLA and RLA, cake layer resistance ratio of RLA over DLA was calculated at 1.35 as shown in equation 25.

$$1.39 \times \frac{(1+\frac{P_{RLA}}{kPa})^{0.72}}{(1+\frac{P_{DLA}}{kPa})^{0.80}} = 1.35 \qquad (25)$$

This ratio is still close to the measured ratio of 1.43 within 6% difference. Incorporating compressibility, predicted specific resistance using equations 19 – 21 were 2.42×10^{13} m/kg for DLA and 3.27×10^{13} m/kg for RLA. Incorporation of compressibility issues results in predictions that are closer, within a factor of 2 but still less than the measured specific resistance values.

Our calculations for Kozeny values are based on fractal dimension measurements that describe the porosity within aggregates (inter porosity). The porosity between aggregates (intra porosity) may also be important after aggregates accumulate and form cake layers on the membrane [75]. The compressibility results shown in Figure 15 can also be used to infer the importance of the porosity between aggregates. Specific resistance values of 5.6×10^{12} m/kg for DLA and 9.0×10^{12} m/kg for RLA at zero pressure are obtained from the Y-axis intercept values of Figure 15. Using these with equations 19 and 21 allows for calculation of an equivalent porosity under zero pressure. The porosity estimates derived from Figure 15 are 9% lower for DLA and 13% lower for RLA than those estimated from equation 20. Values derived from Figure 15 incorporate both intra and inter porosities while values obtained from equation 20 represent only intra porosity estimates and lower overall porosities when intra porosities are accounted for is expected [58]. Porosities were significantly decreased by the cake layer collapse under applied pressure as indicated by the fitted porosity of 0.58, 0.53 for DLA and RLA, respectively. Hence, the change of inter porosity during cake layer collapse appears more significant for estimating specific resistance values than accounting for differences between intra and intra porosities within cake layers. Comparing findings with other studies, fitted porosities are higher than the reported value of ~ 0.4 for C_{60} nanoparticles and Bentonite colloids [76, 77], and specific resistances for both of DLA and RLA are slightly higher than what is reported for aggregated nanoparticles and SiO_2 colloids of 460 nm [72, 77, 78]. Nevertheless, specific resistances of DLA and RLA are lesser than that of Bentonite colloids of 5000 nm; this is in line with predications of equations 19 and 20. In addition, DLA resistance is found to be lesser than that of RLA. This is different from reports for C_{60} nanoparticles [76], but in agreement with others [72, 77-79] and equations 19 and 20.

3.3 Summary and Conclusions

Nanoparticles were aggregated under DLA and RLA regimes to form aggregates of different morphology as quantified by measured fractal dimensions. Aggregate fractal structure differences coincided with measured filtration resistance values. Specific resistance of RLA was 43% higher than that of DLA, and the resistance ratio of RLA over that of DLA was predicted within 6% using only known particle sizes, aspect ratio and measured fractal dimensions. While resistance ratio predictions showed good agreement, measured specific resistance values were 20 times greater

32

than those predicted for both RLA and DLA conditions. Incorporation of compressibility indexes into predictions for specific resistance values improved predictions to within a factor of 2 and remaining prediction errors are attributed to estimated porosities.

A microfiltration rejection of 1 was achieved for both of DLA and RLA regimes in this study and complete nanoparticle removal was accomplished through pre-coagulation at high ionic strength. In order to obtain a porous structure with less resistance, a fast (DLA) coagulation process is suggested for nanoparticle removal.

In this study, Kozeny values were determined from morphology measurements obtained from light scattering of the aggregate suspensions. Due to compressibility and possible rearrangement of aggregates within the cake layer, this nanofluid morphology characterization is inadequate to predict filter performance. To provide better estimates for nanofluid filtration resistance, more information on aggregate structure within the cake layer is necessary. Future studies should investigate the fractal dimension of the cake layer using alternate methods, possibly through dilution and re-suspension of the cake layer deposit after it is formed during the filtration process.

3.3.1 Additional Details of This Study Are Provided in The Following Publications:

Feng, X. and Johnson, D. W. (2013), "Aggregated Nanoparticle Morphology Effects on Membrane Filtration", *Chemical Engineering Communications*, submitted for publication September 2013

Feng, X. (2012). Nanoparticle morphology effects in heat and mass transfer processes, The University of Texas at San Antonio.

3.3.2 Details of This Study Were Provided in These Presentations:

Drew Johnson, Xuemei Feng, Nanoparticle Morphology Effects in Membrane Filtration", the 23rd Annual Meeting of the North American Membrane Society, Boise ID, June 2013

Part (4) Heat Transfer Enhancements and Viscosities of Nanofluids Comprised of Large Aspect Ratio Nanoplatelets.

A key finding of Study 2 was that heat transfer enhancements, for some nanofluids, could be predicted with effective medium theory using nanoparticle aspect ratios. In this study graphene nanofluids, comprised of water and surfactant (2% sodium cholate) and two-dimensional carbon platelet structures were investigated for viscosity and heat transfer capabilities. Graphene nanofluids are of particular interest because graphene exhibits superior thermal conductivity in the range of 2000–5350 W/mK at room temperature, due to the unusual features of two-dimensional phonon heat conduction [80]. Because graphene is naturally unstable in water and tends to aggregate, the use of surfactant is necessary to keep graphene in suspension. Based upon findings to date, graphene at moderate volume fractions of 0.003 can enhance thermal conductivities up to 8% while maintaining nanofluid viscosities near that of pure water.

Effective medium theory incorporating aspect ratios for platelet structures such as graphene, is provided by Chu et al., 2012 [80], and can be used to predicted using to predict the thermal conductivity of graphene water mixtures as provided in equation 26.

$$9(1-f)\left(\frac{K_e-K_m}{2K_e+K_m}\right) = \frac{2Kx}{K_e\left(2^{R_kK_x}/_L+1\right)} + \frac{K_e\left(2^{R_kK_z}/_t+1\right)}{K_z} - 1 \qquad (26)$$

Where K_e is the effective thermal conductivity, K_m is the thermal conductivity of the background medium *i.e.* DI water with 2% w/v Sodium Cholate, f is the solid fraction composition of the solution. K_x is the thermal conductivity in the horizontal-plane, K_z is the thermal conductivity in the vertical plane. $Kx=Kz=2000$W/mK from [80]. R_k is the Kapitza resistance- interfacial thermal resistance. For composites with carbon nanofillers, R_k covers the range of $3 - 9 \times 10^{-8}$m^{2}K/W[80] .

4.1. Experimental Methods

4.1.1. Nanofluid Preparation

Graphene nanoplatelets (Diameter ~5µm, Thickness of 2-10nm) purchased from ACS Material LLC (Medford, MA) were added to a 2% w/v sodium cholate DI water solution at a loading of 27 g L^{-1}. Sodium cholate surfactant was used to prevent graphene aggregation. The nanofluid mixture was sonicated (Digital Sonifier 450, Branson Ultrasonics Corporation, Danbury CT) in a 40 mL borosilicate glass vial for 1-10 hrs at 4 $^{\circ}$C. Temperature control was provided using a water batch circulator (Isotemp 3016 R134A, Fisher Scientific, Hanover Park IL). The resulting exfoliated graphene platelet nanofluid was subsequently centrifuged (Centra-8, International Equipment Company, Chattanooga TN) at 1000 RPM for 10 minutes to provide a stable suspension suitable for thermal conductivity and solution viscosity measurements at different platelet volume fractions.

4.1.2. Volume Fraction Determination

Graphene nanoplatelet volume fractions for different sonication times were determined from absorbance measurements (DR5000, Hach, Loveland CO) at a wavelength of 660 nm with an absorbance coefficient of 141.4 mL mg^{-1} m^{-1}.

4.1.3. Thermal Conductivity Determination

Thermal conductivities were measured over 16 hours with a KD2 pro thermal properties analyzer (±5% accuracy, Decagon Devices, Inc., Pullman, WA) using the transient hot wire method [25]. To perform these measurements, nanofluids were pipetted (Thermo Fisher Scientific Inc., Pittsburgh, PA, 05-403-121) into a 15 mL graduated polypropylene centrifuge tube (Thermo Fisher Scientific Inc., Pittsburgh, PA, 12-565-286B) creating a total volume of 16.7 mL of mixture that excluded any head space when the tube was caped. The probe of KD2 pro analyzer was then inserted into the nanofluid through a hole drilled into the cap and fixed with tape (Thermo Fisher Scientific Inc., Pittsburgh, PA, 15-901-10G). The tube was placed in a plastic rack (Thermo Fisher Scientific Inc., Pittsburgh, PA, 5970-0213), housed in an incubator free of room interference, and the thermal conductivities of nanofluid measured at 25 $^{\circ}$C.

4.1.4. Graphene Imaging

Two-dimensional images of graphene nanoparticles were obtained using SEM. Approximately 10 μL of nanofluids were pipetted onto 300 mesh carbon-coated copper grid (Electron Microscopy Sciences, Hatfield, PA, HC300-Cu 300). Samples were air dried for two hours before capturing images with SEM (Hitachi, South San Francisco, CA, S-5500) in a bright field mode at a voltage of 20 to 30 KV.

4.1.5. Viscosity Measurements

Upon completion of thermal conductivity measurements, nanofluid viscosities were measured using a falling ball viscometer (Cole-Parmer, Vernon Hills, IL, WU-08701-00) at room temperature (23.5 ± 1 ^{o}C). Measurement procedures were for the falling ball viscometer were verified with nanopure water. Nanopure water dynamic viscosity was measured at 0.958 mPa·s; in close agreement with the literature reference value of 0.97 mPa·s [4].

4.2. Results and Discussion

4.2.1. Graphene Dimensions & Aspect Ratio

Morphology of stable nanofluid graphene platelets were observed with SEM. Shown in Figure 16 are SEM image of nanofluids prepared by sonication for 6 hrs. Observed sizes did not change consistently with sonication times and based upon 11 images for samples sonicated between 1 and 10 hrs, average graphene dimensions were platelet length (*L*) of 2.8 um and platelet thickness (*t*) of 47nm.
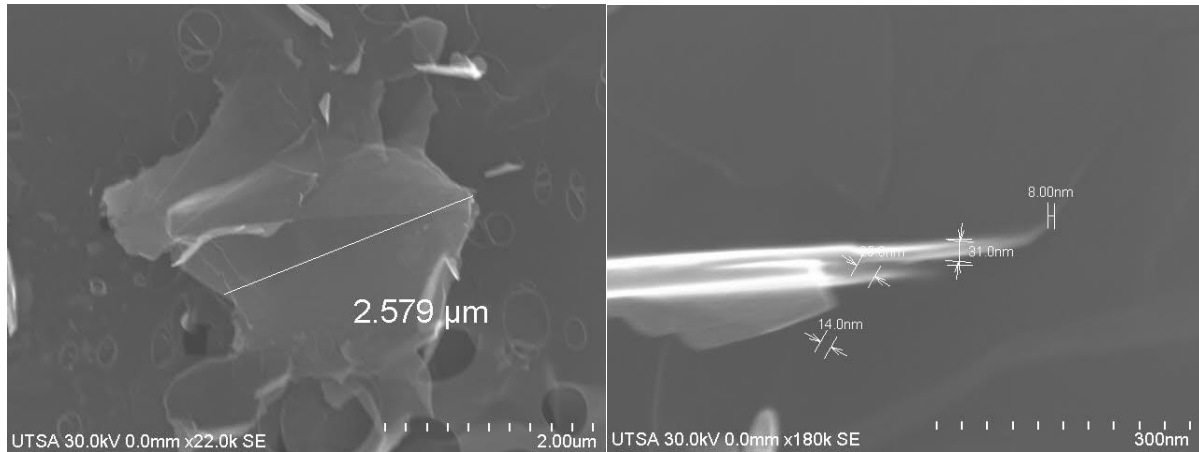

Figure 16- SEM images of graphene platelets after sonication. Left image shows measurement of platelet lengths. Right image shows measurements of platelet thickness.

4.2.2. Graphene Volume Fractions.

Shown in Figure 17 are resulting stable graphene volume fractions for different sonication duration. Highest volume fraction obtained was 0.0027 after 10 hours of sonication. While dimensions

shown in Figure 16 did not change with time of sonication. Stable volume fractions increased with sonication time. Results indicate more particles (higher volume fractions) of sizes that do not settle during centrifuging are created during longer sonication.
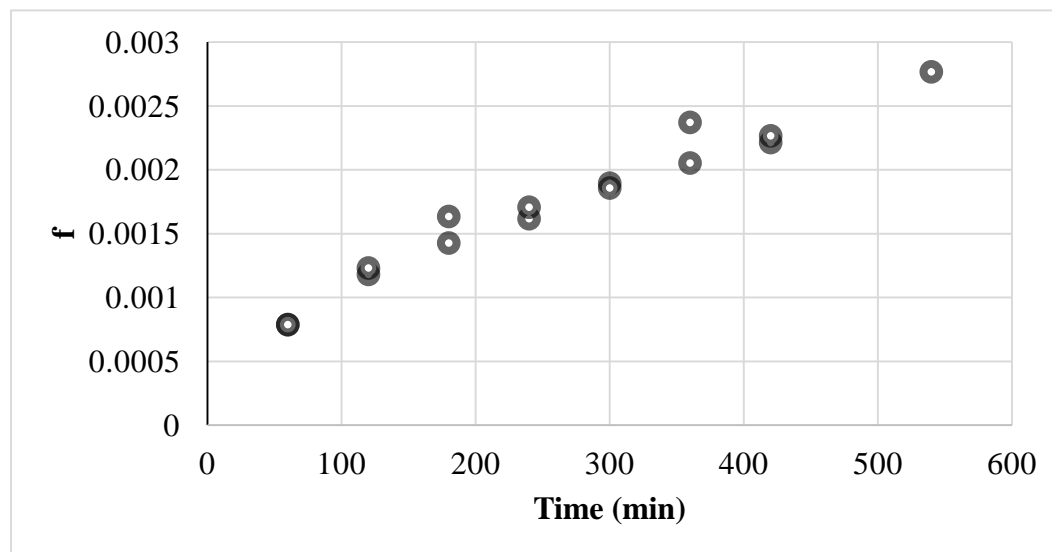

Figure 17- Graphene platelet volume fraction after sonication time.

4.2.3. Graphene Nanofluid Viscosity

Shown in Figure 18 are graphene nanofluid dynamic viscosity. These results require interpretation as the viscosity is constant with increasing nanofluid volume fraction. This is unexpected given that size of particles were found to be constant while volume fraction increased with sonication time. It should be noted that the measured viscosities are all close to that of room temperature water (0.97 mPa·s). Hence, results indicate that volume fractions used in this study are low enough such that measured viscosity values are equivalent to pure water within experimental uncertainty.
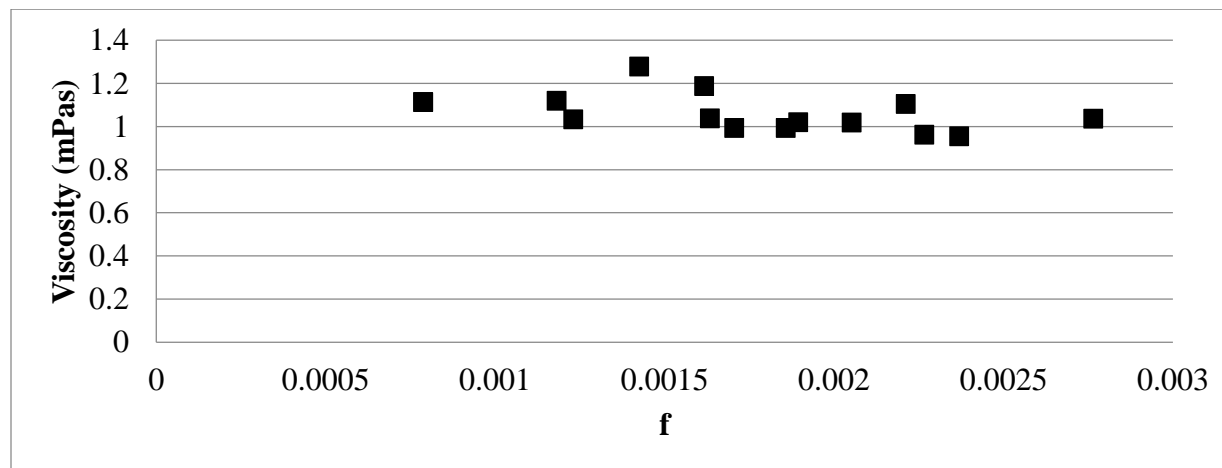

Figure 18 – Graphene nanofluid viscosity for different platelet volume fraction.

36

4.2.1. Measured and Predicted Thermal Conductivities.

Measured and predicted thermal conductivity ratio for the range of volume fractions studied are shown in Figure 19. Measurements fall about the line of prediction from equation 26 with $R_k = 3$ x $10^{-8}m^2K/W$; representing the lower end of resistance values reported by others[80] . Measured and predicted values agree within 6% and scatter within the measured value are attributed to measurement instrument uncertainty of 5%. Furthermore, predicted values are based upon average particle dimensions as determined from SEM imaging. This may not be a true representation of size due to limitations in the numbers of particles analyzed and additional particle size information may be necessary to improve agreement between measured and predicted values. Size information of this type is currently being collected using DLS with a 658 nm laser and a scattering angle of 165° (Beckman Coulter Inc, Brea, CA, Delsa Nano C).
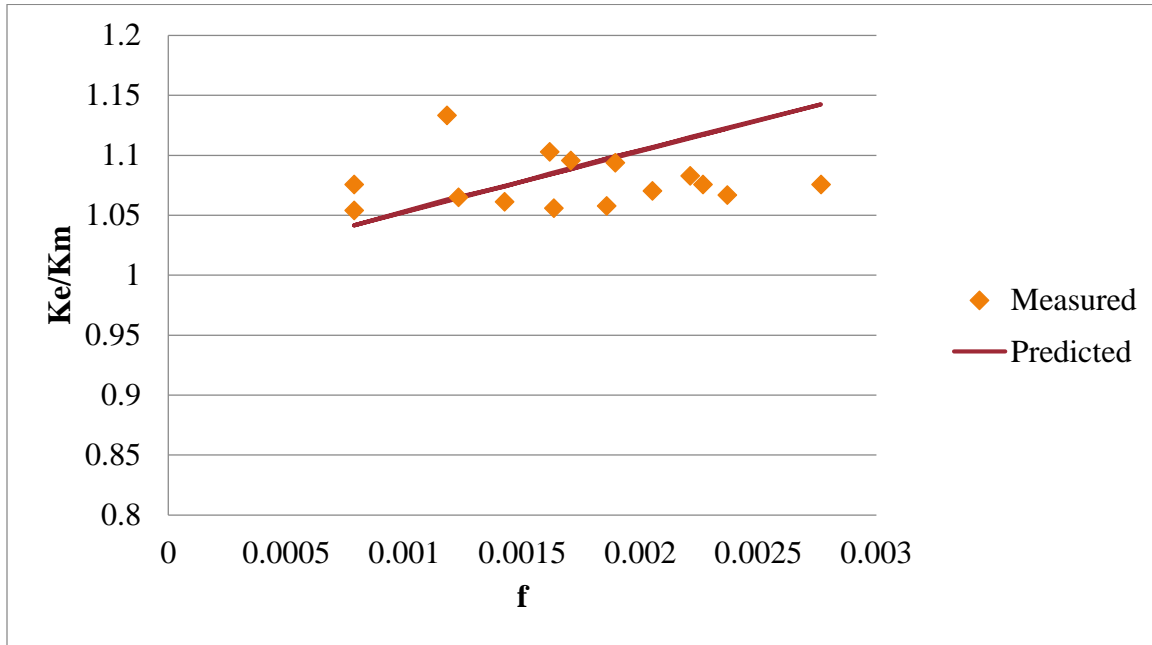

Figure 19-Measured and Predicted Thermal Conductivity Ratios

4.3 Summary and Conclusions

Graphene nanoplatelets (Diameter ~5µm, Thickness of 2-10nm) at a loading of 27 gm L^{-1} were sonicated in a 2% w/v sodium cholate DI water solution. Sodium cholate surfactant was used to prevent graphene aggregation. The resulting exfoliated graphene platelet nanofluid was subsequently centrifuged to provide a stable suspension suitable for thermal conductivity and solution viscosity measurements at different platelet volume fractions. The highest volume fraction achieved of 0.027 (after 9 hours of sonication) provided a thermal conductivity enhancement of 8% with viscosity essentially unchanged and equivalent to water. Measured enhancements in thermal conductivity agree within 6% of effective medium theory predictions based upon nanoplatelet morphologies determined from SEM imaging.

4.3.1 Additional Details of This Study Are Provided in The Following Publication:

Bahaya, B. (2013- In Preparation). Heat Transfer Enhancements and Viscosities of Nanofluids Comprised of Large Aspect Ratio Nanoplatelets, The University of Texas at San Antonio.

References Cited:

1.   Nitsche, J.M. and G. Balgi, *Hindered Brownian Diffusion of Spherical Solutes within Circular Cylindrical Pores.* Industrial & Engineering Chemistry Research, 1994. **33**(9): p. 2242-2247.
2.   Davidson, M.G. and W.M. Deen, *Hindered diffusion of water-soluble macromolecules in membranes.* Macromolecules, 1988. **21**(12): p. 3474-3481.
3.   Rodrigo Riquelme, I.L., Carlos Pérez-López, Juan A Rayas and Ramón Rodríguez-Vera, *Lensless Fourier transform digital holographic interferometer for diffusivity measurement of miscible transparent liquids.* Review of Scientific Instruments, 2009. **80**(5): p. 053106.
4.   Korson, L., W. Drost-Hansen, and F.J. Millero, *Viscosity of water at various temperatures.* The Journal of Physical Chemistry, 1969. **73**(1): p. 34-39.
5.   Bigg, P.H., *Density of water in SI units over the range 0-40°C* Journal of Applied Physics, 1967. **18**(4).
6.   Toda, K. and H. Furuse, *Extension of Einstein's viscosity equation to that for concentrated dispersions of solutes and particles.* Journal of Bioscience and Bioengineering, 2006. **102**(6): p. 524-528.
7.   Fei Duan, D.K., Alexandru Crivoi, *Viscosity affected by nanoparticle aggregation in Al2O3-water nanofluids.* Nanoscale Research Letters, 2011. **6**(248).
8.   Nguyen, C.T., et al., *Temperature and particle-size dependent viscosity data for water-based nanofluids - Hysteresis phenomenon.* International Journal of Heat and Fluid Flow, 2007. **28**(6): p. 1492-1506.
9.   Cussler, E.L., *Diffusion-Mass Transfer in Fluid Systems*. 2009, New York: Cambridge University Press.
10.   Tojo, K., J.A. Masi, and Y.W. Chien, *Hydrodynamic characteristics of an in vitro drug permeation cell.* Industrial & Engineering Chemistry Fundamentals, 1985. **24**(3): p. 368-373.
11.   Komati, S. and A.K. Suresh, *CO2 absorption into amine solutions: a novel strategy for intensification based on the addition of ferrofluids.* Journal of Chemical Technology & Biotechnology, 2008. **83**(8): p. 1094-1100.
12.   Krishnamurthy, S., et al., *Enhanced Mass Transport in Nanofluids.* Nano Letters, 2006. **6**(3): p. 419-423.
13.   Olle, B., et al., *Enhancement of Oxygen Mass Transfer Using Functionalized Magnetic Nanoparticles.* Industrial & Engineering Chemistry Research, 2006. **45**(12): p. 4355-4363.
14.   Zhu, H., B.H. Shanks, and T.J. Heindel, *Enhancing CO-Water Mass Transfer by Functionalized MCM41 Nanoparticles.* Industrial & Engineering Chemistry Research, 2008. **47**(20): p. 7881-7887.

15. Wheeler, A. and A. Ganji, *Introduction to Engineering Experimentation (2nd Edition)*. 2003: Prentice Hall.

16. Turanov, A. and Y. Tolmachev, *Heat- and mass-transport in aqueous silica nanofluids*. Heat and Mass Transfer, 2009. **45**(12): p. 1583-1588.

17. Komati, S. and A.K. Suresh, *Anomalous Enhancement of Interphase Transport Rates by Nanoparticles: Effect of Magnetic Iron Oxide on Gas-Liquid Mass Transfer*. Industrial & Engineering Chemistry Research, 2010. **49**(1): p. 390-405.

18. Veilleux, J. and S. Coulombe, *A total internal reflection fluorescence microscopy study of mass diffusion enhancement in water-based alumina nanofluids*. Journal of Applied Physics, 2010. **108**(10): p. 104316-8.

19. Ozturk, S., Y.A. Hassan, and V.M. Ugaz, *Interfacial Complexation Explains Anomalous Diffusion in Nanofluids*. Nano Letters, 2010. **10**(2): p. 665-671.

20. Fang, X., Y. Xuan, and Q. Li, *Experimental investigation on enhanced mass transfer in nanofluids*. Applied Physics Letters, 2009. **95**(20): p. 203108-3.

21. Fricke, H., *A Mathematical Treatment of the Electric Conductivity and Capacity of Disperse Systems I. The Electric Conductivity of a Suspension of Homogeneous Spheroids*. Physical Review, 1924. **24**(5): p. 575-587.

22. Cherkasova, A.S. and J.W. Shan, *Particle Aspect-Ratio Effects on the Thermal Conductivity of Micro- and Nanoparticle Suspensions*. Journal of Heat Transfer, 2008. **130**(8): p. 082406-7.

23. Li, K., et al., *Aggregation kinetics of CeO2 nanoparticles in KCl and CaCl2 solutions: measurements and modeling*. Journal of Nanoparticle Research, 2011. **13**(12): p. 6483-6491.

24. Chen, K.L., S.E. Mylon, and M. Elimelech, *Aggregation Kinetics of Alginate-Coated Hematite Nanoparticles in Monovalent and Divalent Electrolytes*. Environmental Science & Technology, 2006. **40**(5): p. 1516-1523.

25. Healy, J.J., J.J. de Groot, and J. Kestin, *The theory of the transient hot-wire method for measuring thermal conductivity*. Physica B+C, 1976. **82**(2): p. 392-408.

26. Venart, J.E.S. and R.C. Prasad, *Thermal conductivity of water and oleum*. Journal of Chemical & Engineering Data, 1980. **25**(3): p. 196-198.

27. Thomson, G.H., et al., *Perry's Chemical Engineers' Handbook. Section 2, Physical and Chemical Data*. 2008: McGraw-Hill. 521p.

28. Buongiorno, J., et al., *A benchmark study on the thermal conductivity of nanofluids*. Journal of Applied Physics, 2009. **106**(9): p. 094312-14.

29. Ramires, M.L.V., et al., *Thermal conductivity of aqueous sodium chloride solutions*. Journal of Chemical & Engineering Data, 1994. **39**(1): p. 186-190.

30. Einstein, A., *Investigations on the theory of the brownian movement*. 1915, E. P. Dutton and Company Publishers.

31. Xu, R. *Application Note Determining Particle Shape Using Photon Correlation Spectroscopy Technology*. Available from: https://www.beckmancoulter.com/wsrportal/bibliography?docname=Particle%20Shape%20from%20PCS.pdf.

32. Hassellöv, M., et al., *Nanoparticle analysis and characterization methodologies in environmental risk assessment of engineered nanoparticles*. Ecotoxicology, 2008. **17**(5): p. 344-361.

33. Berne, B.J. and R. Pecora, *Dynamic Light Scattering: With Applications to Chemistry, Biology, and Physics*. 1976 New York: Wiley-Interscience.

34. Bushell, G.C., et al., *On techniques for the measurement of the mass fractal dimension of aggregates.* Advances in Colloid and Interface Science, 2002. **95**(1): p. 1-50.

35. Vicsek, T., *Fractal Growth Phenomena*. 2nd ed. 1999 Singapore: World Scientific.

36. U.S. National Institutes of Health, B., Maryland, USA. Available from: http://rsb.info.nih.gov/ij/.

37. Murr, M.M. and D.E. Morse, *Fractal intermediates in the self-assembly of silicatein filaments.* Proceedings of the National Academy of Sciences of the United States of America, 2005. **102**(33): p. 11657-11662.

38. Wang, W. and Y. Chau, *Self-assembled peptide nanorods as building blocks of fractal patterns.* Soft Matter, 2009. **5**(24): p. 4893-4898.

39. Lee, C. and T.A. Kramer, *Prediction of three-dimensional fractal dimensions using the two-dimensional properties of fractal aggregates.* Advances in Colloid and Interface Science, 2004. **112**(1-3): p. 49-57.

40. Kaszuba, M., et al., *Measuring sub nanometre sizes using dynamic light scattering.* Journal of Nanoparticle Research, 2008. **10**(5): p. 823-829.

41. Lin, M.Y., et al., *Universal reaction-limited colloid aggregation.* Physical Review A, 1990. **41**(4): p. 2005.

42. Lin, M.Y., et al., *Universal diffusion-limited colloid aggregation.* Journal of Physics: Condensed Matter, 1990. **2**(23): p. 5283.

43. Gao, J.W., et al., *Experimental Investigation of Heat Conduction Mechanisms in Nanofluids. Clue on Clustering.* Nano Letters, 2009. **9**(12): p. 4128-4132.

44. Hong, J. and D. Kim, *Effects of aggregation on the thermal conductivity of alumina/water nanofluids.* Thermochimica Acta, 2012. **542**(0): p. 28-32.

45. Shalkevich, N., A. Shalkevich, and T. Buˆrgi, *Thermal Conductivity of Concentrated Colloids in Different States.* The Journal of Physical Chemistry C, 2010. **114**(21): p. 9568-9572.

46. Yoo, D.-H., et al., *Thermal Conductivity of Al2O3/Water Nanofluids.* Journal of the Korean Physical Society, 2007. **51**: p. S84-s87.

47. Carman, P.C., *Fundamental principles of industrial filtration—A critical review of present knowledge.* Trans. Inst. Chem. Eng., 1938. **16**: p. 168-188.

48. Li, X.-Y. and B.E. Logan, *Permeability of Fractal Aggregates.* Water Research, 2001. **35**(14): p. 3373-3380.

49. Veerapaneni, S. and M.R. Wiesner, *Hydrodynamics of Fractal Aggregates with Radially Varying Permeability.* Journal of Colloid and Interface Science, 1996. **177**(1): p. 45-57.

50. Guan, J., R. Amal, and T.D. Waite, *Effect of aggregate size and structure on specific resistance of biosolids filter cakes.* Water science and technology : a journal of the International Association on Water Pollution Research, 2001. **44**(10): p. 215-220.

51. Choo, K.-H. and C.-H. Lee, *Membrane fouling mechanisms in the membrane-coupled anaerobic bioreactor.* Water Research, 1996. **30**(8): p. 1771-1780.

52. Happel, J., *Viscous flow in multiparticle systems: Slow motion of fluids relative to beds of spherical particles.* AIChE Journal, 1958. **4**(2): p. 197-201.

53. Psoch, C. and S. Schiewer, *Resistance analysis for enhanced wastewater membrane filtration.* Journal of Membrane Science, 2006. **280**(1-2): p. 284-297.

54.   Brown, G.R., *Creeping flow of fluids through assemblages of elliptic cylinders and its application to the permeability of fiber mats*. 1975, Institute of Paper Science and Technology: appleton

55.   Happel, J., *Viscous flow relative to arrays of cylinders.* AIChE Journal, 1959. **5**(2): p. 174-177.

56.   Kuwabara, S., *The Forces experienced by Randomly Distributed Parallel Circular Cylinders or Spheres in a Viscous Flow at Small Reynolds Numbers.* Journal of the Physical Society of Japan, 1959. **14**(4).

57.   Xu, W., S. Chellam, and D.A. Clifford, *Indirect evidence for deposit rearrangement during dead-end microfiltration of iron coagulated suspensions.* Journal of Membrane Science, 2004. **239**(2): p. 243-254.

58.   Antelmi, D., et al., *Cake Collapse in Pressure Filtration.* Langmuir, 2001. **17**(22): p. 7137-7144.

59.   Koroleva, L., *Abrasive properties of aluminum iron oxide nanoparticles.* Inorganic Materials, 2009. **45**(10): p. 1158-1165.

60.   Feng, X. and D. Johnson, *Characterization of dispersed and aggregated Al2O3 morphologies for predicting nanofluid thermal conductivities.* Journal of Nanoparticle Research, 2013. **15**(6): p. 1-11.

61.   Mu, H., Y. Chen, and N. Xiao, *Effects of metal oxide nanoparticles (TiO2, Al2O3, SiO2 and ZnO) on waste activated sludge anaerobic digestion.* Bioresource Technology, 2011. **102**(22): p. 10305-10311.

62.   Jiang, W., H. Mashayekhi, and B. Xing, *Bacterial toxicity comparison between nano- and micro-scaled oxide particles.* Environmental Pollution, 2009. **157**(5): p. 1619-1625.

63.   Chen, K.L. and M. Elimelech, *Aggregation and Deposition Kinetics of Fullerene (C60) Nanoparticles.* Langmuir, 2006. **22**(26): p. 10994-11001.

64.   Johnson, P.N. and A. Amirtharajah, *Ferric chloride and alum as single and dual coagulants.* Journal (American Water Works Association), 1983. **75**(5): p. 232-239.

65.   Lee, J.-D., et al., *Effect of Coagulation Conditions on Membrane Filtration Characteristics in Coagulationâˆ’Microfiltration Process for Water Treatment.* Environmental Science & Technology, 2000. **34**(17): p. 3780-3788.

66.   Lee, S.A., A.G. Fane, and T.D. Waite, *Impact of Natural Organic Matter on Floc Size and Structure Effects in Membrane Filtration.* Environmental Science & Technology, 2005. **39**(17): p. 6477-6486.

67.   Davis, M.L., *Water and wastewater engienering design principles and practice*. 2011, New York: McGraw-Hill.

68.   Carpineti, M., et al., *Salt-induced fast aggregation of polystyrene latex.* Physical Review A, 1990. **42**(12): p. 7347-7354.

69.   Hackley, V.A. and M.A. Anderson, *Effects of short-range forces on the long-range structure of hydrous iron oxide aggregates.* Langmuir, 1989. **5**(1): p. 191-198.

70.   Zhang, J. and J. Buffle, *Multi-method determination of the fractal dimension of hematite aggregates.* Colloids and Surfaces A: Physicochemical and Engineering Aspects, 1996. **107**(0): p. 175-187.

71.   Hurd, A.J. and D.W. Schaefer, *Diffusion-Limited Aggregation in Two Dimensions.* Physical Review Letters, 1985. **54**(10): p. 1043-1046.

72.   Waite, T.D., et al., *Colloidal Fouling of Ultrafiltration Membranes: Impact of Aggregate Structure and Size.* Journal of Colloid and Interface Science, 1999. **212**(2): p. 264-274.

73.   Sørensen, B.L. and P.B. Sorensen, *Applying cake filtration theory on membrane filtration data.* Water Research, 1997. **31**(3): p. 665-670.
74.   Am Ende, D.J. *Chemical Engineering in the Pharmaceutical Industry R & D to Manufacturing*. 2011; Available from: http://public.eblib.com/EBLPublic/PublicView.do?ptiID=624518.
75.   Park, P.-K., C.-H. Lee, and S. Lee, *Permeability of Collapsed Cakes Formed by Deposition of Fractal Aggregates upon Membrane Filtration.* Environmental Science & Technology, 2006. **40**(8): p. 2699-2705.
76.   Henry, C. and J.A. Brant, *Mechanistic analysis of microfiltration membrane fouling by buckminsterfullerene (C60) nanoparticles.* Journal of Membrane Science, 2012. **415– 416**(0): p. 546-557.
77.   Mendret, J., et al., *In situ dynamic characterisation of fouling under different pressure conditions during dead-end filtration: Compressibility properties of particle cakes.* Journal of Membrane Science, 2009. **333**(1–2): p. 20-29.
78.   Zhang, J., et al., *Influence of azo dye-TiO2 interactions on the filtration performance in a hybrid photocatalysis/ultrafiltration process.* Journal of Colloid and Interface Science, 2013. **389**(1): p. 273-283.
79.   Chellam, S. and W. Xu, *Blocking laws analysis of dead-end constant flux microfiltration of compressible cakes.* Journal of Colloid and Interface Science, 2006. **301**(1): p. 248-257.
80.   Chu, K., et al., *Modeling the thermal conductivity of graphene nanoplatelets reinforced composites.* EPL (Europhysics Letters), 2012. **100**(3): p. 36001.